Dependence of Degradation Mechanisms in Magnesium Alloys on Grain Orientation and Interfaces in 3D

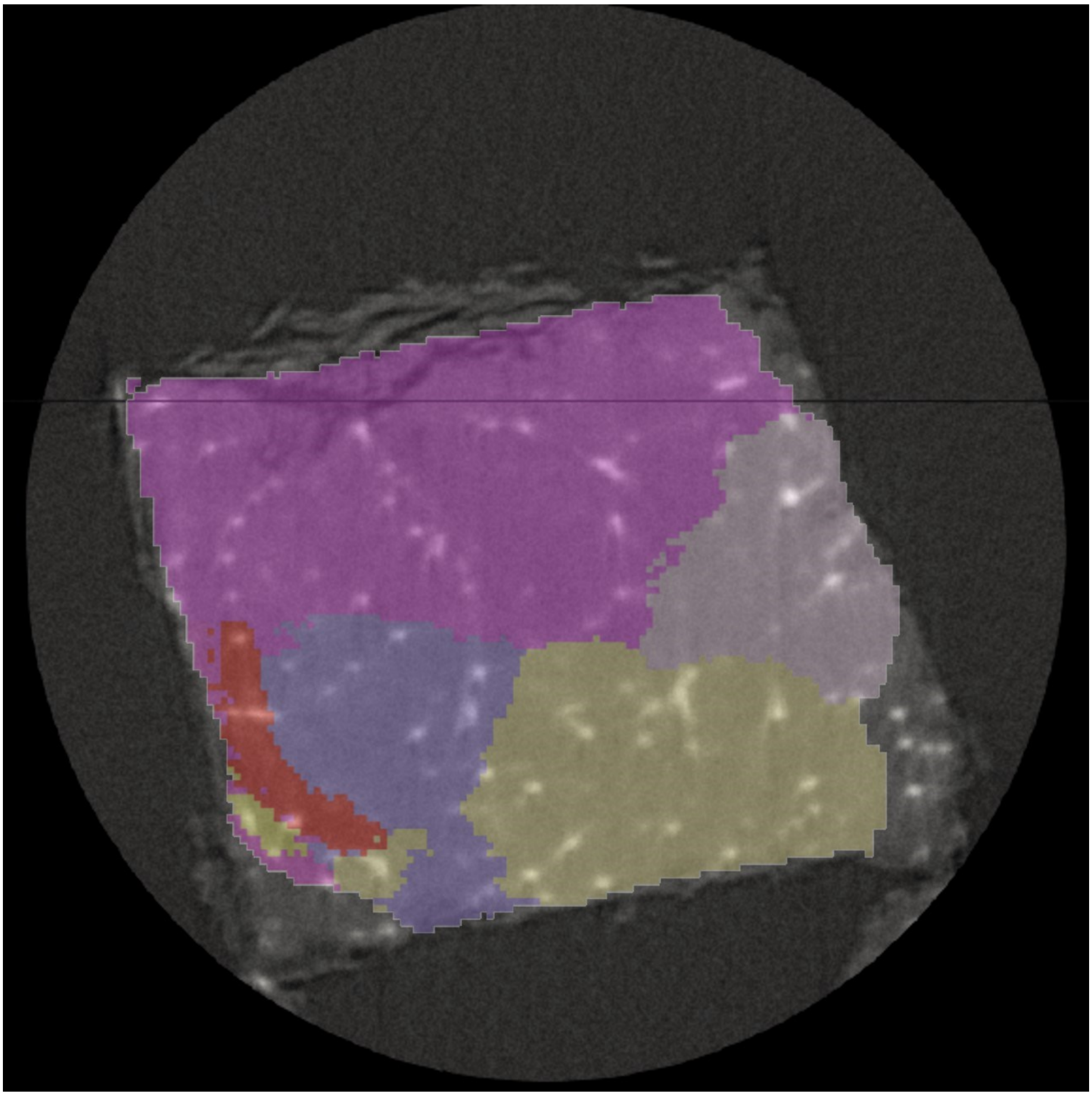

Johan Ranstad

Division of Mechanics, Materials and Component Design

Department of Mechanical Engineering Sciences

Master’s Thesis 2024

Cover picture: Absorption contrast of Z5 AS overlaid with the reconstruction of grains from diffraction contrast. Imaging by Diffraction Contrast Tomography.

Dependence of degradation mechanisms in Magnesium Alloys on Grain Orientation and Interfaces in 3D

Master's Thesis

Johan Ranstad

Division of Mechanics, Materials and Component Design

Department of Mechanical Engineering Sciences

Lund University 2024

Examiner: PhD. Rikard Hjelm

Supervisor: Professor Dmytro Orlov

Co-Supervisor: Professor Lars Wadsö

Division of Mechanics Material and Component Design
Department of Mechanical Engineering, LTH
Ole Römers väg 1
P.O. Box 118
SE-221 00, Lund, Sweden

MSc Thesis

ISRN LUTFD2/TFMT—23/5068--SE

Department of Mechanical Engineering Sciences

Lund University

Ole Römers väg 1

P.O. Box 118

SE-221 00, Lund, Sweden

SWEDEN

Printed in Sweden

Lund 2024

Abstract

Magnesium alloys are promising candidates as biomedical implants. However, a good understanding of their degradation processes is lacking. In this work, degradation in two magnesium alloys were studied in a simple physiological-fluid electrolyte of H_2O+0.9*wt%*NaCl, Mg-5*wt%*Zn (Z5) & Mg-5*wt%*Zn-0.3*wt%*Ca (ZX50). Z5 alloy was studied in two microstructural states, as-cast and as a supersaturated solid solution. Degradation rate and enthalpy were determined using hydrogen gas evolution and isothermal calorimetry, respectively. Diffraction contrast tomography was then used to assess the dependence of grain orientation during degradation of the Z5 material in both the microstructural states by immersion tests in the same electrolyte. Corrosion was observed over the entire samples. Specific regions were identified where the samples were more corroded. These regions showed affinity for both local microstructural properties as well as certain crystallographic orientations.

Keywords: *Mg-Zn alloys, Diffraction contrast tomography, Isothermal Calorimetry, Immersion testing, Corrosion Rate, Microgalvanic coupling.*

Sammanfattning

Magnesiumlegeringar är lovande kandidater till biomedicinska implantat för behandling av bland annat benbrott, då de naturligt och ofarligt bryts ned i kroppen. Dock saknas en god förståelse om hur nedbrytningsprocessen går till. Detta arbete studerar nedbrytningsprocessen av två magnesiumlegeringar, Mg-5*wt%*Zn (Z5) och Mg-5*wt%*Zn-0.3*wt%*Ca (ZX50), i fysiologisk saltlösning, H_2O + 0.9*wt%*NaCl. Z5 legeringen studerades i två mikrostrukturella tillstånd; som gjuten och som en övermättad fastfaslösning. Nedbrytningshastighet bestämdes via mätning av vätgasutveckling kopplad med en isotermisk kalorimeter.

Den mikrostrukturella påverkan av nedbrytningsprocessen utreddes för legering Z5 i båda tillstånden via diffraktionskontrasts-tomografi via nedsänkningstest i samma elektrolyt. Specifika regioner där proverna korroderade mer aggressivt identifierades och påvisades ha affinitet för både lokala mikrostrukturella betingelser och kristallografiska orienteringar.

Populärvetenskaplig sammanfattning - En metall för att spara en operation

Idag används stål eller titan som fixtur för benbrott. Dessa måste opereras in, och efter läkning opereras ut igen. En kandidat att ersätta dessa material är Magnesium, vilken naturligt och ofarligt bryts ned i kroppen så en andra operation inte behövs.

För att kunna designa en magnesiumlegering vilken kan användas som implantat vid benbrott måste vi förstå hur nedbrytningsprocessen går till. Förstår vi detta så kan man spara in på en operation och alla risker och kostnader den medför.
I den magnesiumlegering som detta arbete studerat har det visats att det är två faktorer som i huvudsak påverkar var och hur fort materialet bryts ned:

- Hur tätt packade atomerna är i de korn som bryts ned
- Hur de pyttesmå klumparna av iblandade ämnen är spridda

Metaller byggs upp av atomer vilka sitter på specifika platser i ett gitter. I dessa gitter kan plan av atomer definieras och vissa i plan sitter atomerna tätare. Där atomerna sitter tätare är de starkare bundna till varandra och därmed är det svårare för dessa att lossna i en nedbrytningsprocess.

När en metall stelnar från en smälta bildas flera av dessa gitter-system samtidigt till det ordnade gittret, dessa olika system kallas korn. Varje korn har sina plan pekandes på sitt sätt. Detta gör att ett material kan få olika egenskaper beroende på hur de olika kornen är orienterade, till exempel kan ett lager där atomerna inte sitter så tätt lättare reagera med något i omgivningen.
Ett fenomen av de olika riktningarna bland kornen är att röntgenstrålar studsar i olika mönster ifrån korn beroende på i vilka riktningar planen pekar, detta gör det möjligt att ifrån mönstren baklänges se hur kornen sitter och i vilka riktningar kornens plan pekar.

Smälts flera metaller tillsammans och sedan stelnar bildas en legering, en mix av metallerna. De olika metallerna där i har olika egenskaper, till exempel hur hårt de håller i sina elektroner (mäts i elektronegativitet). Under tiden som legeringen stelnar kommer lokala skillnader göra att vissa pyttesmå klumpar med en annan sammansättning och egenskaper än bulkmaterialet bildas, ungefär som luftbubblor i isbitar. Den egenskap som spelar störst roll i nedbrytningen av en metall är elektronegativiteten. En sådan klump med en högre elektronegativitet än bulkmaterialet kommer dra åt sig elektroner från bulkmaterialet, vilket gör att bulkmaterialet börjar genomgå en kemisk reaktion vilket är nedbrytningen. Detta är faktiskt samma process som gör att batterier fungerar. Magnesium, vilket är bulkmaterialet, har lägre elektronegativitet än alla rimliga legeringskandidater.

Ska en metall tillverkas för att användas i kroppen är det viktigt att ha koll på så att allt som är där i är ofarligt. Magnesium, Zink och Kalcium är exempel på metaller som vi naturligt redan har i kroppen, de finns även som kosttillskott på mataffär eller apotek. Zink och Kalcium har båda högre elektronegativitet än Magnesium.

Tidigare forskning har visat att vi faktiskt kan påverka hur stora kornen är via vilka andra ämnen man legerar med, Kalcium gör till exempel kornen mindre.
Det visar även att de ytor av kornen som hamnar utåt kan vi påverka genom hur man framställer och bearbetar legeringen. Detta tar oss ett steg närmare att skapa en metall för att spara en operation.

Glossary and abbreviations

Å:	Ångström (unit: 10^{-10} m)
APD:	Atomic Packing Density
AS:	As Supplied, in reference to microstructural state
BCC:	Body-Centered Cubic
BSE:	Backscatter Electrons
DCT:	Diffraction Contrast Tomography
ΔH:	Reaction Enthalpy
DI:	Deionized water
dn/dt:	Corrosion rate
dp/dt:	Pressure change rate
DWS:	Diamond Wire Saw
EBSD:	Electron Backscatter Diffraction
EDS:	Energy Dispersive Spectroscopy
HCP:	Hexagonal Close Packed
i-Cal:	Isothermal Calorimetry
IPF:	Inverse Pole Figure
Mg:	Magnesium
MgO:	Magnesium Oxide
$Mg(OH)_2$:	Magnesium (di-)Hydroxide
µm:	micrometer (unit: 10^{-6} m)
NaCl:	Sodium Chloride
SE:	Secondary Electrons
SEM:	Scanning Electron Microscope
SiC:	Silicon Carbide sanding paper
SSSS:	Supersaturated Solid Solution
Wt. %:	Weight percentage
Z5:	Mg - 5Zn alloy (*wt. %*)
ZX50:	Mg - 5Zn - 0.3Ca alloy (*wt. %*)

List of figures

Table of Contents

1. Introduction

1.1 Overview

Magnesium is the lightest engineering metal with a density of 1.74 g/cm^3 and the eight most abundant element in the earth's crust making it a very interesting candidate for different engineering applications (Polmear et al., 2017).

Magnesium is considered a good candidate as a biomedical implant material, (Witte 2015). Present implants for treating bone fractures are made of non-degradable steel or titanium alloys and degradable polymers. These may release toxic particles as they degrade inside the body Another negative aspect of using steels and titanium alloys is their relatively high stiffness in comparison to natural bone. A implant stiffer than the surrounding bone will bear a higher load than the bone structure, this leads to a decrease in local bone density through a process known as stress shielding, (Frost, 1994).
Comparatively magnesium and magnesium alloys have an elastic modulus more similar to that of bones which would negate this effect (Staiger et al., 2006).

One of the main obstacles for the wide use of magnesium implants is that the degradation rate of magnesium in typical *in vivo* conditions is quite high. Along with the degradation, significant amounts of hydrogen gas is produced during the corrosion process. Gas evolution and pressure build-up may harm body tissue (Witte et al., 2005). If a bio-absorbable material with a corrosion rate that matches the regeneration rate could be designed, a second surgery to remove the supportive structure for the regeneration would be unnecessary. Since surgical procedures naturally carries health risks and costs, this would be a most beneficial improvement.

Magnesium exhibits anisotropic properties, both physically and chemically, hence the crystallographic structure and texture is of interest when studying corrosion properties of magnesium materials (Vinogradov 2023, Orlov et al., 2011) .

The dependence of corrosion behaviour on crystallographic orientations and grain interfaces must therefore be carefully explored to be able to tailor properties of Mg alloys. This work utilizes immersion tests in combination with Differential contrast tomography to study the effects of crystallographic orientation on corrosion behaviour in magnesium alloys. This is correlated with in-house developed isothermal calorimetry set-up at the Department of Mechanical Engineering Sciences to compare degradation rates of the materials studied.

1.2 Aim

The aim for this thesis project is to analyse the dependencies of grain orientation and grain interfaces on corrosion rates in selected Mg alloys in aqueous media.

The techniques utilized in this work are Differential Contrast Tomography (DCT) Isothermal Calorimetry (i-Cal) and Scanning electron microscopy (SEM).

1.3 Limitations

Due to the scope and time available for current work DCT scans were analyzed for Z5 materials while calorimetric measurements were done for all three materials, Z5 AS, Z5 SSSS & ZX50.

2. Background

2.1 Magnesium and its alloys

Magnesium is available at high purities, above 99.8%, but is seldom used as a pure material for engineering purposes. The hexagonal structure and atomic diameter (3.2 Å) allow a large range of solute elements, such as Aluminium, Zinc, Calcium, Silver, Thorium, Yttrium, Cerium, Zirconium etc. (Polmear et al., 2017, Esmaily et al., 2017 & Atrens et al., 2020).

Magnesium alloys are used extensively in engineering applications where light weight and high strength is required. Such applications are for example the frame of a car seat, gearboxes, and nuclear applications, (Polmear et al., 2017).

No internationally accepted code of naming Mg alloys exists, but the method, ASTM B275, used by the American Society for Testing Materials, ASTM, is getting more and more use. The method uses letters to describe alloying elements and numbers to describe the nominal composition in weight % of the alloying elements. The letters come in descending order corresponding to alloying contents.
The following letter code is used:
A – Aluminium, B – Bismuth, C – Copper, D – Cadmium, E – Rare Earth elements, F –Iron, G – Magnesium, H – Thorium, J – Strontium, K – Zirconium, L – Lithium, M – Manganese, N – Nickel, P – Lead, Q – Silver, R – Chromium, S – Silicon, T – Tin, W – Yttrium, X – Calcium, Y – Antimony, Z – Zinc.
The magnesium content is assumed to be of bulk content hence names does not always start with G. If the alloying contents are in equal amounts the letters are in alphabetical order.
Examples of names in this nomenclature are AZ91, indicating the alloy Mg-9Al-1Zn, WE43, indicating an alloy of Mg-4Y-3*Rare Earth* & Z5 indicating the alloy Mg-5Zn (Polmear et al., 2017).

Magnesium – aluminium alloys are widely studied due to excellent castability, good corrosion resistance and reasonable mechanical properties at room temperature. However, Aluminium is neurotoxic and the accumulation of Al from degradation of an implant alloy can induce neurological diseases, hence Al free alloys are desired to minimize risks (El-Rahman 2003 & Jiang et al. 2020).

Zinc is the second most common alloying element in magnesium alloys and is also an essential element for biological functions in the human body making it a more promising alloying candidate for biomedical applications of magnesium alloys (Jiang et al. 2020). The Mg-Zn binary phase diagram is presented in Figure 1.

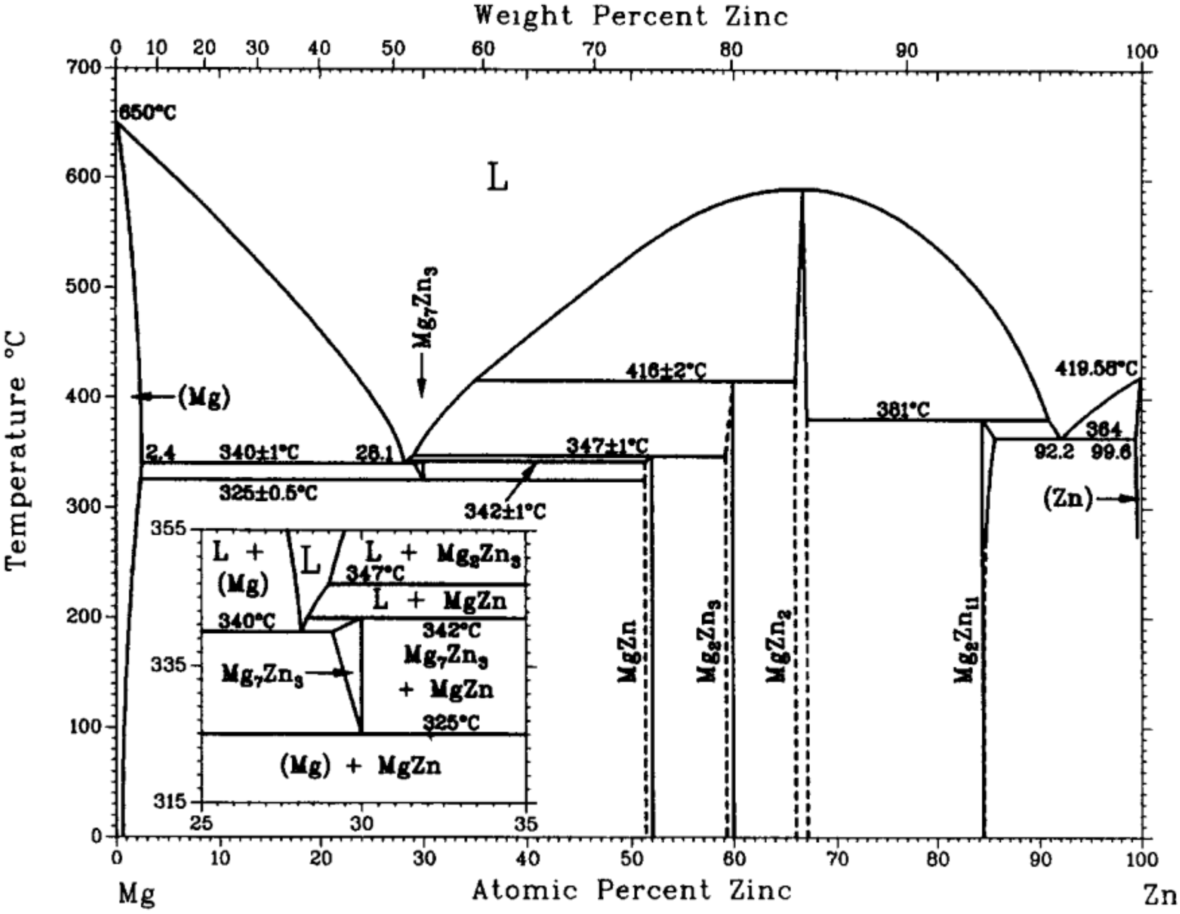

Figure 1: Mg-Zn Binary phase Diagram, (Bahn et al. 1993).

From the binary phase diagram, it is visible that the maximum solubility of Zinc in magnesium is relatively high (6.2 *wt.*%) at an elevated temperature of 325 °C (Polmear et al. 2017). At lower temperature the maximum solubility of Zn drops to 1.6 *wt.*%, the dissolved Zn contributes to solid solution strengthening and the remaining Zn will form intermetallic phases as precipitate particles in the solid solution matrix. It is believed that the intermetallic precipitates (Mg_xZn_y) provide an age hardening effect on the material (Jiang et al. 2020). But it is believed that these intermetallic precipitates play a detrimental role in corrosion (Esmaily et al. 2017).

The materials studied in this project contains 5 *wt. %* Zn. These materials should contain a secondary phase of precipitated intermetallic particles with a higher Zn concentration, Mg_7Zn_3, than the background matrix according to the phase diagram.

Magnesium and Mg-alloys have clear anisotropic mechanical properties that are influenced by the means of production and/or mechanical treatments. The reason behind the anisotropic behaviour is due to the hexagonal packing structure. This results in different properties along different crystallographic axis in the material and surfaces show crystallographic texture, (Shi et al., 2022). In this work, the point of interest is if such a mechanical anisotropy also affects corrosion behaviour.

2.2 Biomedical Magnesium

Magnesium alloys have been extensively studied as potential biomedical implant alloys due to their biocompatibility, biodegradability, and mechanical properties (Staiger et al., 2006 & Witte et al., 2005, Maier et al., 2019). Magnesium is a biocompatible metal that is essential for numerous physiological processes in the human body, and it can be metabolized and excreted without causing harm to the body (Staiger et al., 2006).

One of the main advantages of magnesium alloys as implant materials is their biodegradability, which means that they can gradually degrade and be absorbed by the body over time, eliminating the need for a second surgery to remove the implant (Staiger et al., 2006, Zhang et al., 2014). This is especially advantageous for temporary implants, such as those used in orthopaedic surgery to stabilize fractures or in cardiovascular surgery to repair blood vessels (Staiger et al., 2006).
In addition to their biodegradability, magnesium alloys also have favourable mechanical properties, such as high strength-to-weight ratio, good ductility, and low density, which makes them attractive for use in biomedical applications (Staiger et al., 2006 & Zhang et al., 2017). For example, magnesium alloys have been studied as potential materials for orthopaedic implants, such as bone plates, screws, and pins, as well as for cardiovascular stents (Staiger et al., 2006). Commercially available implants fully certified already exists from companies such as BIOTRONIK, Syntellix AG and U&i (BIOTRONIK AG, Syntellix AG & U&i).

However, magnesium alloys also have some limitations that must be addressed before they can be widely used as biomedical implant alloys. One of the main challenges is their relatively rapid degradation rate in the body, which can cause inflammation and other adverse reactions (Staiger et al., 2006 & Chen et al., 2019). This degradation rate can be controlled through alloy design or controlling the size and shape of the implant (Staiger et al., 2006).

Overall, magnesium alloys have shown promise as biomedical implant alloys due to their biocompatibility, biodegradability, and mechanical properties (Staiger et al., 2006 & Witte et al., 2005). Ongoing research is focused on optimizing their properties and developing new techniques to improve their performance as implant materials (Staiger et al., 2006, Chen et al., 2019, Vinogradov et al., 2023, Esmaily et al., 2017).

2.2.1 Magnesium corrosion in aqueous environments

Corrosion of magnesium has been studied extensively, (Esmaily et al., 2017, Witte et al., 2005, Witte 2011, Atrens et al., 2020, Jiang P et al., 2020, Song 2011). In this work the corrosion behaviour of Mg-alloys in aqueous environments is of interest as this is the environment present in biomedical applications.

The corrosion of Mg-alloys occurs in many complex reactions depending on environment and corrosive media, (Esmaily 2017, Vinogradov 2023, Mei et al., 2020). The most stable product forming during corrosion is $Mg(OH)_2$ (Song et al. 2020).

Magnesium hydroxide may form in a single step reaction:

$$Mg(s) + 2H_2O(l) \rightarrow Mg(OH)_2(s) + H_2(g) \qquad \Delta H^0 = -353.00\ kJ/mol \qquad \text{(R1)}$$

It may also form through multiple step reactions producing intermediate magnesium oxide, MgO:

$$Mg(s) + H_2O(l) \rightarrow MgO(aq/s) + H_2(aq/g) \qquad \Delta H^0 = -315.41\ kJ/mol \qquad \text{(R2)}$$

$$MgO(aq/s) + H_2O(l) \rightarrow Mg(OH)_2(aq/s) \qquad \Delta H^0 = -37.6\ kJ/mol \qquad \text{(R3)}$$

Or by dissolving ions, Mg^{2+} and OH^-, and precipitation of products:

$$Mg(s) + 2H_2O(l) \rightarrow Mg^{2+}(aq) + 2OH^-(aq) + H_2(g) \qquad \Delta H^0 = -355.19\ kJ/mol \qquad \text{(R4)}$$

$$Mg^{2+}(aq) + 2OH^-(aq) \rightarrow Mg(OH)_2(s) \qquad \Delta H^0 = 2.19\ kJ/mol \qquad \text{(R5)}$$

Additionally, other reactions may occur producing other oxides hydroxides depending on available species in the system, (Orlov et al. 2020). Reaction enthalpies are noted as negative values here as to indicate the spontaneous reaction. Further in this work enthalpies will be noted in absolute values.

From all presented reaction systems above, (1)-(5), it can be noted that hydrogen gas, H_2 (g) is produced at a one-to-one molar ratio of reacted magnesium. This is used later in the experimental setup as it provides an additional way of measuring the extent of reaction in a gas tight system (Orlov, Viklund & Wadsö 2022).

It has been reported that different crystallographic planes on surfaces and interfaces show different corrosion behaviour. The reason for this is the anisotropic lattice unit cell of Magnesium. However, different publications have reported conflicting results on the matter. For example, McCall et al. (2005) studied a single crystal sample of magnesium exposed to an aqueous solution containing 0.01 M NaCl with the addition of dichromate. They showed that the basal plane (0001) had the lowest resistance to corrosion and that corrosion propagates along certain crystallographic directions in a filamentary-like fashion. Contrary to these findings, Shin et al., (2012) also studied single crystal magnesium where the basal plane showed the highest resistance to corrosion. A study by Liu et al., (2008) on coarse grained polycrystalline magnesium with well characterized crystallographic orientations of the grain structure noted anisotropy of corrosion properties that depends on crystallographic orientations. This research reported similar findings to Shin et al. (2012), that the basal plane (0001) showed the highest resistance to corrosion. In fine-grained magnesium, the orientation of individual grains did not have a noticeable effect on the corrosion behaviour, but the effect of crystallographic texture was still noticeable. Gerashi et al., (2022) accredits these contradictions to the formation of a passivating film. This film builds up on the surface and its features strongly depend on external conditions such as the presence of passivating agents in the solution or the aggressiveness of the corrosive media used. They noted that the presence of passivating elements in the solution increased the likelihood of filament-like corrosion, which was reported by McCall et al., (2005). These findings denote the importance of experimental conditions when designing corrosion tests on magnesium and magnesium alloys, as it seems the experimental conditions might influence the results more than the properties of the material. It also highlights that the dependence of crystallographic texture on corrosion behaviour still unknown in magnesium and magnesium alloys.

2.2.2 Corrosive media selection

Many studies on magnesium corrosion have been performed using different corrosive media, no standard setup has universally been agreed upon, (Mei et al., 2020). This creates differences in published results on corrosion resistances and rates of magnesium and Mg-alloys. The different corrosive media used can be classified into five categories with increasing complexities: simple isotonic saline solution (NaCl 0.9 *wt. %*), balanced salt solutions such as Ringer's or PBS, more advanced saline solutions such as Hanks balanced salt solution (HBSS), Earle's balanced salt solution (EBSS) or simulated body fluid (SBF) containing phosphates and carbonates. These three are all inorganic media. To further mimic *in vivo* conditions, cell culture media that also contains organic compounds such as amino acids, vitamins, glucose, antibiotics, and pH indicators/buffeters have been tested. Finally in the most advanced solutions proteins are also added (Mei et al., 2020).

To date, there are no standardized procedures for producing the named solutions (SBF, HBSS, EBSS, etc.), resulting in that what one paper refers to as SBF might not be identical to SBF used in another publication. The issue of inconsistency and trends of complexity in corrosive media selection is extensively discussed by Mei et al., (2020).

It is shown in multiple review papers that corrosion rates generally decrease with increasing complexity of the corrosive media (Mei et al., 2020, Vinogradov et al., 2023, Esmaily 2017). In isotonic saline solution, the presence of Cl^- interferes with the equilibrium of forming $Mg(OH)_2$ as the Cl^- ions compete with OH^- in reacting with dissolved Mg^{2+}. However, $MgCl_2$ is highly soluble in water, resulting in the dissociation to ionic form, Mg^{2+} and Cl^-, again where Mg^{2+} might react with OH^- to form $Mg(OH)_2$. As through this process it would be the ionised species that react, the reaction would not take place on the surface and no protective film would form. The presence of Cl^- ions will then increase the overall corrosion rate (Bornapour et al., 2016).

In corrosive media containing more ionic species, like Ringer's solution or PBS, more side reactions similar to the interactions with Cl^- ions are possible. This does not need to further accelerate the corrosion behaviour in the media as some salts precipitate on the surface and form protective films on the corroding surface, (Vinogradov et al., 2023).

More complex ions, e.g., phosphate and carbonate, have been shown to coordinate to Mg^{2+} ions in a chelating manner. This also alters the equilibrium of the corrosion reactions as well as physically inhibits the surface of exposed specimen (Viklund 2020 & Mei et al., 2020).

More complex solutes in the electrolyte such as organic compounds further decrease corrosion rates due to more side reactions and chelation effects being possible. Proteins such as albumin, which has commonly been used in solutions to mimic serum, has been shown to effectively act as an inhibitor of bio-corrosion slowing down corrosion rates by a factor up to 100 (Vinogradov et al., 2023).

In summary, the reason for decreasing corrosion rates with increasing electrolyte complexity are competing side reactions as well as physical inhibition of interfaces (Mei et al., 2020, Viklund 2020, Vinogradov 2023 & Esmaily 2017).

Based on this trend, along with the notation that Na^+ and Cl^- are ions already present in the human body, it was decided to use the simplest isotonic saline solution of 0.9 *wt.%* NaCl in this project. This should allow focusing the study on the mechanisms of Mg alloy corrosion minimizing the role of species precipitating from a medium.

2.3 Analytical methods

The three main analytical methods used in this work are Isothermal calorimetry (I-cal), Diffraction contrast tomography (DCT) and Scanning Electron Microscopy (SEM).

2.3.1 Isothermal Calorimetry

In this work, isothermal calorimetry is used to gauge the extent of corrosion reactions and the degradation rates of the sample materials. An isothermal calorimetric cell consists of two chambers, one reference chamber and one sample chamber, a sketch presented in Figure 2 below.

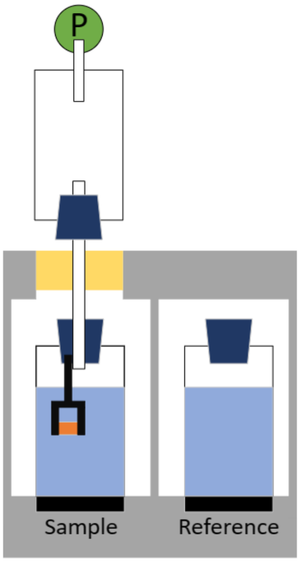

Figure 2: Schematic illustrating calorimetric cell, with the sample chamber containing a sample vial filled with electrolyte (light blue) and a sample (orange) mounted in a sample holder(black). A tube through the plug connects the sample vial to a pressure sensor (green).

Isothermal calorimeter is designed to ensure temperature stabilisation in each chamber to keep both sample and reference at the same temperature. The thermal power required to maintain temperature is recorded. This is proportional to the rate of corrosion by a factor of enthalpy:

$$P = \frac{dn}{dt} \cdot \Delta H \qquad \text{(E1)}$$

Where P is thermal power (W), dn/dt is corrosion rate and ΔH is the total reaction enthalpy. The thermal power is recorded over the length of the experiment.

As was mentioned in section 2.2.1, the molar ratio of reacted Mg to produced H2 is 1:1. By applying the ideal gas law, the corrosion rate of Mg can then be calculated as a function of change in pressure:

$$\frac{dn}{dt} = \frac{dp}{dt} \cdot \frac{V}{R \cdot T} \qquad \text{(E2)}$$

Where dn/dt is the corrosion rate, dp/dt is a change in pressure due to H_2 gas evolution, V is the total gas volume of the system, R is the universal gas constant, and T is the temperature of the system. Since V, R & T are constants in the system, collecting the evolved hydrogen and measuring the pressure change over time, the corrosion rate can be calculated.

Using pressure evolution as a measure of corrosion rate is advantageous compared to other methods such as conventional gravimetric or electrodynamic methods as it can be continuously preformed to monitor the reaction process with minimal influence on the sample, (Orlov, Viklund & Wadsö 2022).

2.3.2 Scanning Electron Microscopy

In this work, Scanning Electron Microscopy (SEM) is used to determine the microstructure of the materials used as well as sample surfaces before and after exposure to corrosive media. SEM is a powerful technique that is well established in material science and engineering to investigate the microstructure and surface properties of materials. In SEM, a beam of high-energy electrons is generated and focused on the surface of a sample, causing various signals to be emitted from the interaction volume of the sample. These signals include secondary electrons (SE) and backscattered electrons (BSE) among others, a schematic of a SEM and interaction volume of a sample is shown in figure 3.

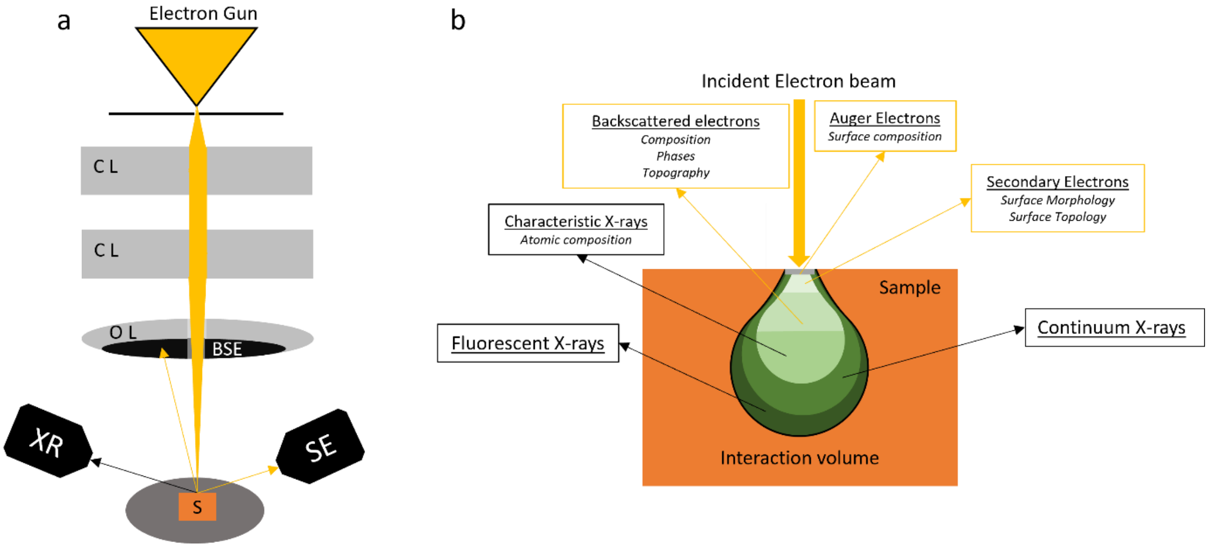

Figure 3:(a) SEM schematic with Electron gun, C L: Condenser Lens, O L: Objective Lens, S: sample, BSE: BSE detector, SE: SE detector and XR: X ray detector. (b): interaction volume of incident electron beam and sample.

Different interactions of electrons and the material makes it possible to analyse differences in phases, structures, and atomic number of the studied material. More information on this is available in Goldstein et al., 2003, Reimer and Kohl, 2008, and Williams and Carter, 2009.

2.3.3 Diffraction contrast tomography

Diffraction contrast tomography, DCT, is a non-destructive method to study microstructure and crystallography of materials in three dimensions (3D). DCT combines X-ray diffraction and computed tomography to obtain information of both the microstructure and three-dimensional crystallographic structure of a sample.

In DCT, a sample is rotated in an X-ray beam and two datasets, absorption contrast and diffraction pattern, are recorded at each angle. The absorption contrast is used to visualize the microstructure of the sample, similar to BSE in SEM, but in 3D (Sun et al. 2022). The diffraction pattern contains information on crystallographic orientations of the sample. Diffraction occurs at specific scattering angles (2θ) corresponding to the orientation of crystallographic planes and their lattice spacing (*d*). Diffraction spots will be visible where the wavelength (λ) fulfils Bragg's law, $\lambda = 2\mathrm{d}\sin(\theta)$. From this, the collected diffraction patterns can be used to reconstruct the lattice structure corresponding to the diffraction pattern. By rotating the sample and collecting a diffraction pattern at multiple angles the crystallographic structure can be recreated in 3D, (McDonald et al., 2015). This technique allows imaging of individual grains or areas/volumes of interest in a sample. A description of the DCT setup is shown in figure 4 below. In this work, DCT will be combined with immersion testing. Reconstruction of the grain structure from collected data was done with help from Stephen Hall, Department of construction science, Lund University, using GrainMapper3D™ software by XnovoTech™ (Xnovotech).

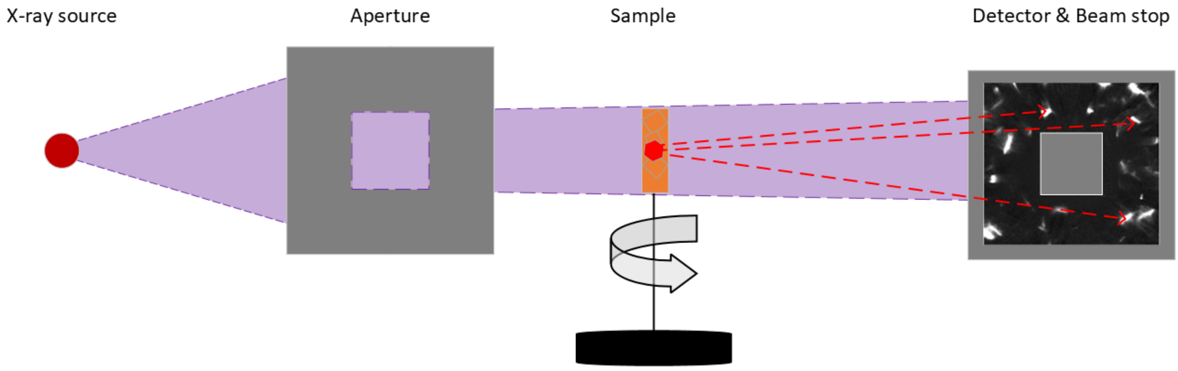

Figure 4: Schematic of DCT operation set up (a), adapted from McDonald et al., 2015; and diffraction pattern from sample Z5 SSSS (b), as explained in detail below.

3. Methods and Materials

In this project, one binary Mg - 5Zn (*wt.%*), Z5, and one ternary Mg - 5Zn - 0.3Ca (*wt.%*), ZX50, alloys were studied. The binary Z5 alloy was studied in two different microstructural states, as cast (AS) and a super-saturated solid solution (SSSS). The ternary ZX50 alloy was only studied as cast (AS). To confirm the microstructural state of both Z5 alloys, SEM analysis was performed, as the solution treatment was not the part of a present work.

The electrolyte used for the corrosion testing was 0.9 *wt.%* NaCl. Preparation procedures and equipment used is described in the following sections.

3.1 Sample preparation

Specimens of the materials were prepared carefully following the procedures described below.

3.1.1 Rough cutting of samples

Specimens were cut from as-supplied work pieces of varying rectangular shapes to desirable sizes; thin plates about 10 x 5 x 1 mm, using the Accutom-5 disc-blade saw, figure 5A. A SiC cut-off wheel (Struers™ 10S15) was used. Cutting was performed at a rotational speed of 3000 RPM of the cutting disk, and a sample feed speed of 0.1 mm/s.

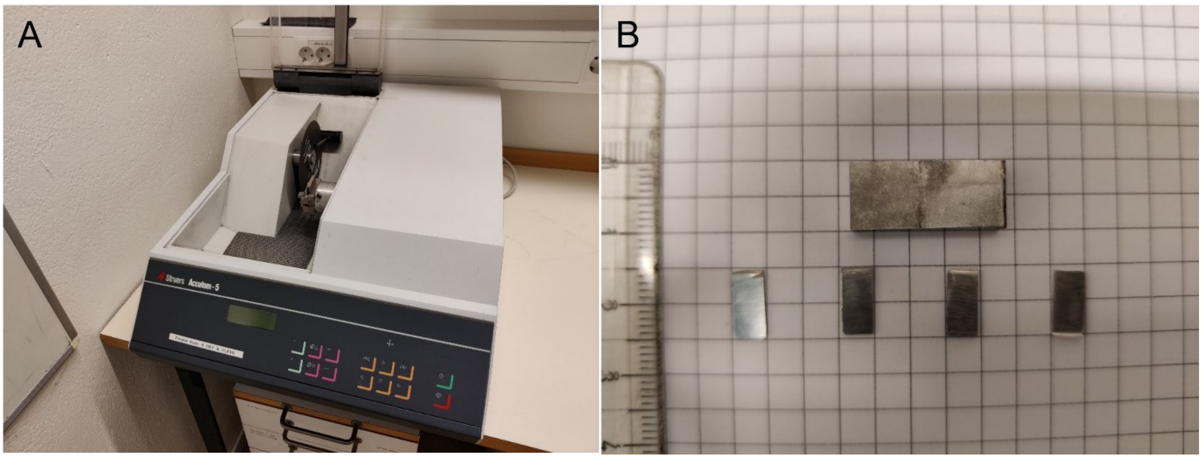

Figure 5: Equipment used for sample cutting. A: Accutom-5 disc-blade Saw, B: as-cut specimens (Z5 AS).

The first cut of approximately 5 mm from the edge of as-supplied material was discarded to guarantee parallel cut surfaces of the specimen. Since the cutting-wheel is water-cooled, specimen requires further preparations to remove the potentially formed corrosion layer on their surfaces.

3.2 Corrosion medium (electrolyte)

The corrosion medium used as electrolyte in this work was selected as isotonic saline solution, 0.9 *wt.* % NaCl. The simplest solution was selected for two reasons: to reduce possibilities of interfering and competing side reactions/mechanisms and that the simplest solution has been documented to show the highest corrosion rates. This selection will hence model the upper limit of corrosion rates of the studied materials (Mei et al., 2020). The corrosive medium was prepared as follows:

- 100 ml DI water was added to a 1000 ml beaker, magnetically stirred.
- 9 g NaCl was weighted and gradually added to the beaker during stirring.
- Stirring continued until no visible NaCl remained in the beaker.
- 900 ml DI water was added to the beaker while stirring.
- Stirring continued for 5 minutes.
- Resulting solution was bottled in a glass container and stored at ambient temperature.

3.3 Isothermal Calorimetry

Isothermal calorimetry is one of the main techniques used in this project. The setup used calorimetric cells coupled with pressure sensors. The calorimeter used in this work is the TAM Air 4 by Thermometric. The instrument is equipped with eight channels, of which only four were used at a time. The pressure sensors used were Motorola MPX5100. The cover of the calorimeter had undergone a re-design to accommodate for the pressure sensor setup. The schematic of calorimetric cell setup is shown in figure 6. To ensure high fidelity of our results, the instrument was re-calibrated prior to the measurements in this project.

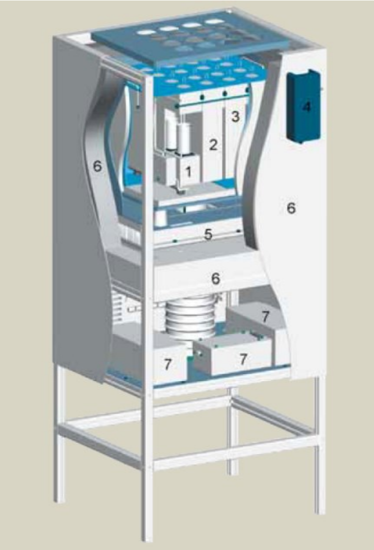

Figure 6: TAM Air isothermal calorimeter showing; three of the eight calorimeter channels (1-3), one with the heat sink removed to show the ampoule holders for sample and reference (1). Temperature controller (4), Peltier element (5), insulation (6) and data-logger and power supply (7), (Wadsö 2005).

3.3.1 Specimen preparation – calorimetry

For each material sample, four specimens were produced and examined with isothermal calorimetry. Specimen were first cut using the Accutom-5 saw, as described above. Each specimen was then grinded on SiC paper with increasing grit in four steps: P500, P1200, P2000 and P4000. Between each step the specimen was washed with water, dried with ultraclean air. When moving up one grit the sample was rotated 90°, according to standard operation practices, to simplify visual inspection and the progression of grinding. After the final step of grinding on P4000 paper, the sample was washed in an ultrasonic bath submerged in ethanol. The final step of grinding (P4000) was always performed as close to mounting and measurement as possible, see section 3.3.3.

3.3.2 Baseline recording

A reference baseline was needed to be recorded before each measurement. The goal of the baseline recording is to mimic the test environment as close as possible to the experiment but without any reaction, i.e. a sample present. Such a procedure allows better differentiation of signal from noise.

Initially four reference 20 mL glass vials containing only electrolyte were prepared by adding to each vial 17 mL of electrolyte, measured by volume (using a pipette) and controlled by weight (17g). These vials were then wiped clean on the outside to remove any residual electrolyte, closed with rubber stoppers and mounted in the reference chambers of the calorimeter. The reference vials were replaced with new electrolyte solution if a new batch of electrolyte solution was prepared.

Following this, four identical vials were prepared with electrolyte for the sample chambers. While sealing these vials with the rubber stoppers, a tiny amount of vacuum oil was applied to the rubber stopper to ensure no gas leakage. The sample vial was connected to the preassembled pressure sensor vial by a thin metal pipe running through the rubber stopper. The specimen holder was also mounted in the rubber stopper to mimic the live setup as close as possible.

As the reference vials were kept in the calorimeter (37°C), and the electrolyte was stored at ambient temperature (20°C), precautions to reduce the thermal shock to the system was needed. After filling the sample vials with electrolyte, they were stored on a heating plate set at 37°C for the time required to fill all the vials. The vials were then taken from the heating plate and placed in the calorimetric cells in the same order as they were filled.

Experimental data were recorded on a separate control PC connected to both thermal sensors and pressure sensors using PicoLog PLW data logger. The software automatically logs channel data over time and stores it as a *.PLW file, which can be exported as a *.csv file through the software.

The baseline was recorded for at least 24 hours to match or slightly exceed the intended sample recording time. The vials and holders for calorimetric measurements are presented in figure 7.

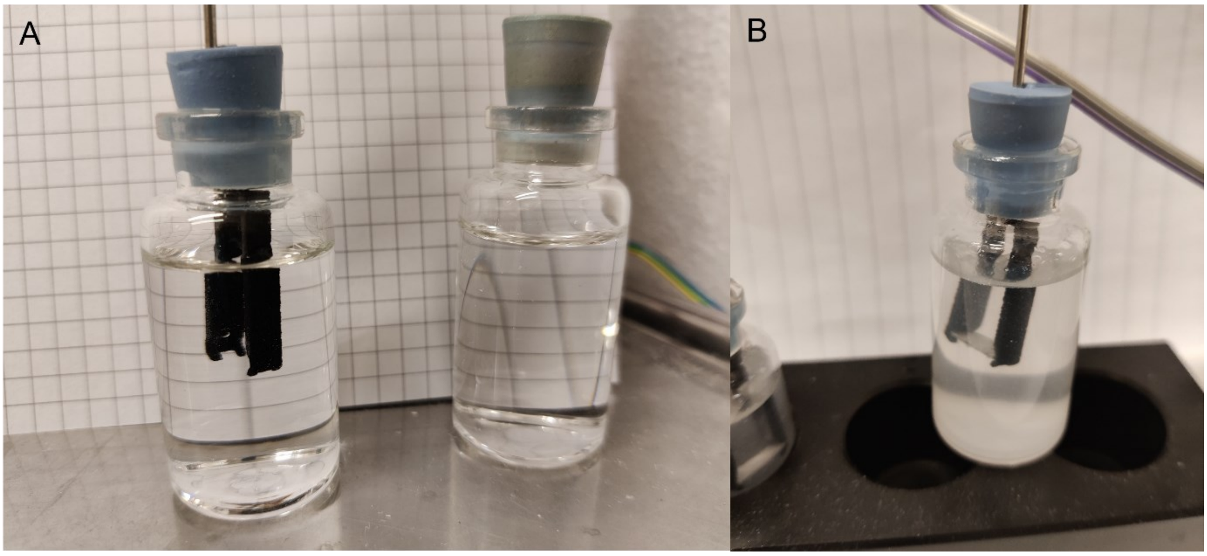

Figure 7: Calorimetric vials. A: sample vial (left) and reference vial (right) prepared for baseline recording. B: Sample vial with mounted sample (post-test).

To ensure as close as possible relation between baseline and measurement, the electrolyte solution of the sample vial was not renewed between baseline and measurement recording.

3.3.3 Mounting and Measurement

The specimens were prepared as described in section 3.3.1. This was done in parallel to the baseline recording up until, but not including the final step of grinding. Since the corrosion reaction is heavily dependent on temperature, it was crucial to mount the specimens in the test vials as quickly as possible as the test vials needed to, for a short time, be removed from the calorimeter. Hence, the final grinding step, at P4000, was done within the last hour of baseline recording. After all specimens were polished and sonicated in ethanol, they were individually measured in all three dimensions. Five measurements of each dimension, height width and thickness, were taken using a calliper. The highest and lowest value were regarded as outliers and discarded, the mean value of the three remaining measurements were used to calculate the surface area of each specimen. The measurements of each specimen are presented in table A1, appendix 1.

The experimental data were recorded in the same way as described for the baseline above, see section 3.3.2.

3.3.4 Data Analysis

Since the data output from the isothermal calorimeter are in voltage differentials, further data processing was needed to recalculate from voltage to relevant quantities. A python script was built in-house and made available for this purpose from previous projects (Viklund 2020, Fragrkakis 2023, Reinwalt & Tayeb-Bey 2019).

3.4 Diffraction Contrast Tomography

Diffraction contrast tomography (DCT) was the main analytical technique used in this project. The instrument was ZEISS Versa XRM520 at the 4D Imaging Lab, Department of construction science, LTH, Lund University.

3.4.1 Specimen preparation - DCT

For DCT scans, samples were first pre-cut at the Accutom –5 saw to half the thickness described in 3.1.1, to a rectangular shape of approximately 0.5 x 10 x 10 mm^3. The pre-cut sample was then further cut using a diamond wire saw, figure 8 A, to a square rod approximately 0.5 x 0.5 x 10 mm^3. To perform this cut, the sample was mounted on a plate using adhesive wax (T_m = 80°C), figure 8 B. The wire was lubricated and cooled using water-free synthetic oil to prevent corrosion during cutting. The first rod of approximately 2 mm cut from the edge was discarded to ensure parallel cut surfaces. The specimen used is shown in figure 8 C.

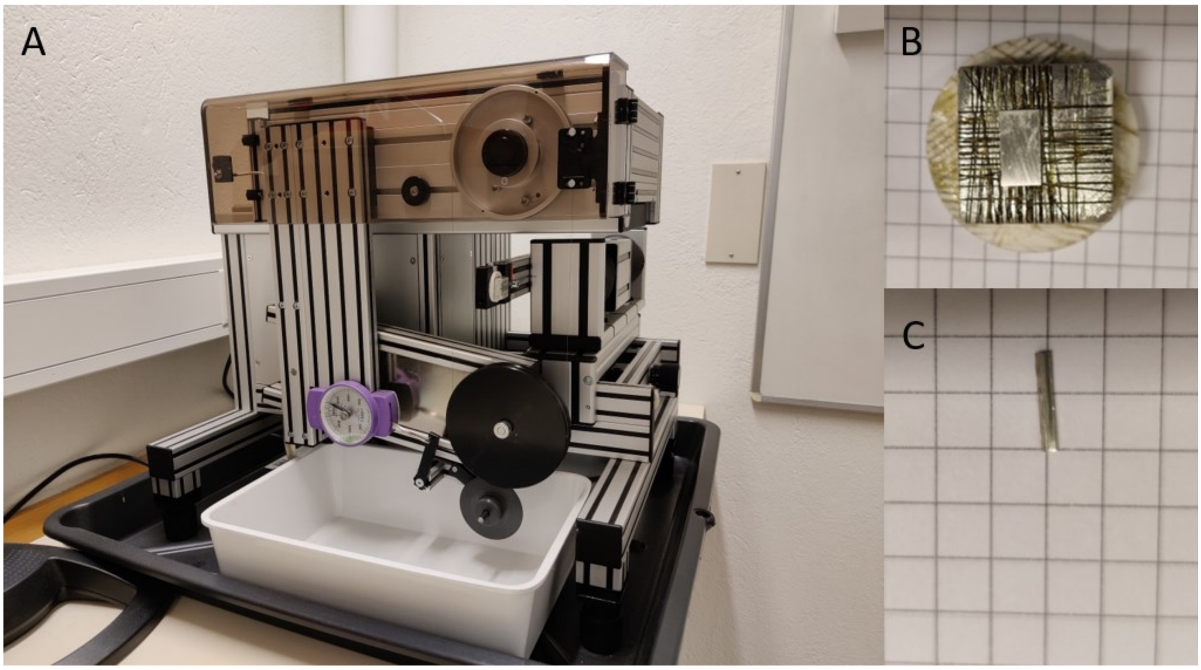

Figure 8: Sample preparation Diamond Wire Saw A: Diamond wire saw with mounted specimen holder. B: Specimen holder with mounted specimen attached using adhesive wax. C: Produced specimen.

The surface of the specimens produced was not prepared any further to keep the microstructure of the specimen and not induce texture. Any flash on cut edges were left untouched. The diamond wire saw was used in this work since it allows producing extremely delicate cuts minimizing subsurface damage and thus alterations in corrosion behavior of the specimens.

3.4.2 Measurements

For each sample, two measurements were taken, one before and one after 24 hours of exposure to the electrolyte. The setup used to expose the samples to the electrolyte is shown in figure 9 below.

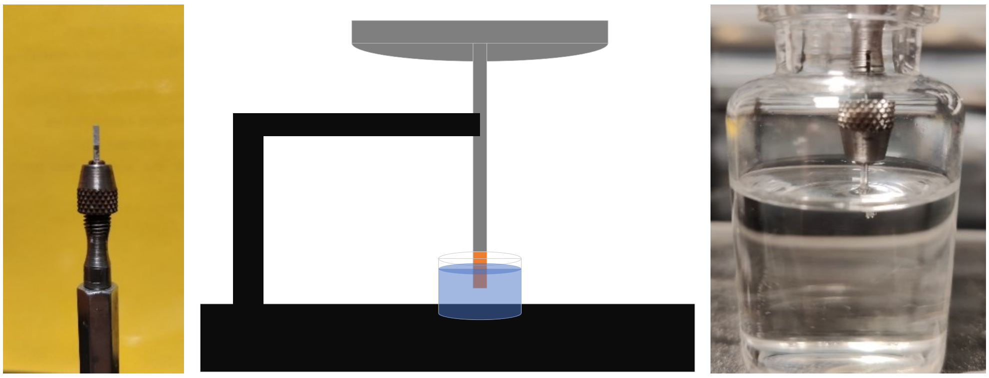

Figure 9: DCT exposure setup. Left: Specimen mounted on holder for DCT measurements, middle: schematic of exposure setup, right: Specimen during exposure to the electrolyte.

For all the samples, one initial absorption scan to review the entire sample volume was taken before exposure to the electrolyte, as a reference. This allowed revealing the microstructure of the initial samples for comparison and illuminating the same volume of the sample pre- and post-exposure. The volume of interest was chosen to not include the tip of the specimen as that might become lost during the exposure to the electrolyte. The volume of interest could not be too far from the tip to ensure that during exposure the electrolyte did not come into contact with more electropositive holder potentially altering the expected chemical reactions. The volume of interest was defined by a known distance from the sample holder in the scan volume.

The region of interest was scanned in both modes, absorption and diffraction, prior to the exposure. Post-exposure, the *diffraction* scan was not performed since the grain structure in the volume of interest does not change during corrosion. The build-up of corrosion product could potentially also interfere with the reconstruction (data post-processing) as the unit cell structure for corrosion product differs from that of non-corroded sample. The reconstructions were carried out based on pure magnesium, $a=b=3.2093$ Å, $c=5.2103$ Å, $\alpha=\beta=90°$, $\gamma=120°$, as the alloys if interest in this project are substitutional type solid solutions.

In comparison to the isothermal calorimetric experiments, no thermostatic sample environment at 37°C was available at the location of the DCT equipment. The immersion for DCT was thus performed at 28°C in a chamber with monitored temperature. Such a difference is considered acceptable since the difference in the temperature of measurements between isothermal calorimetry and DCT scanning affects only the kinetics (and not types) of chemical reactions.

3.5 SEM

To examine the microstructural states of the Z5 and ZX50 alloys, SEM imaging was used. The SEM instrument used was FEI Quanta 200 MKII operated at 20 kV in both SE and BSE modes. During the analysis of DCT data, it was considered important to identify the secondary phase in Z5 and ZX50 by energy dispersive spectroscopy (EDS).

3.5.1 Specimen preparation

Specimens were prepared for SEM analysis through the same grinding procedure presented in section 3.3.1 above. After the grinding, the samples were further hand-polished on cloth disks in four steps, three using diamond-particle suspension with particle sizes of 3, 1 and ¼ µm. Water-free lubricant was used to prevent corrosion during preparation. In-between each step, the specimen was washed using ethanol and dried with ultraclean air. The fourth and final polishing step was performed using a suspended silica particle solution, 0.04 µm, OP-S. Removing remaining silica particles from the sample surface proved hard, requiring another method besides rinsing with ethanol. Rinsing was thus complemented with an ultrasonic bath, using ethanol, which provided satisfactory results. If too much silica particles remained on the surface after this cleaning process, specimen was polished again with the suspended silica solution and washed again until a satisfactory result was achieved.

The polished specimen was mounted on a sample-holder using conductive carbon tape. Imaging settings is presented in the images taken, see figure 10 in 4.1.

4. Results

The results are split in three parts, starting from the SEM imaging, following by isothermal calorimetry and finally the results from the DCT are presented.

4.1 SEM analysis

Main goal of the SEM imaging was an initial assessment of the microstructure of the material samples to be studied with DCT. The images taken are presented in figure 10

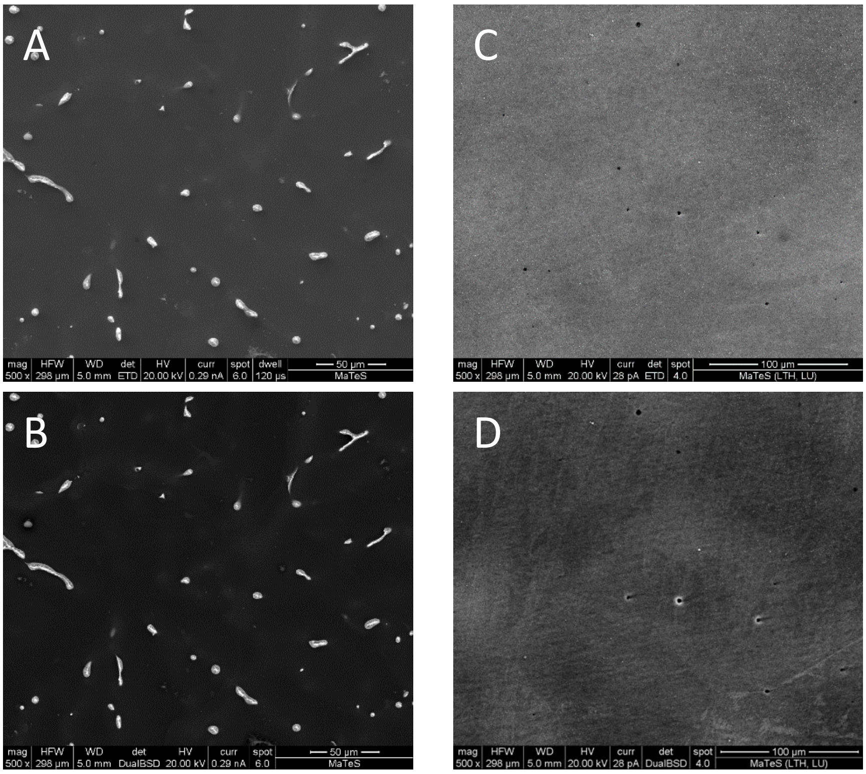

Figure 10: SEM images of Z5 alloy taken at 500x magnification. A: Z5 AS – SE. B: Z5 AS – BSE. C: Z5 SSSS – SE. D: Z5 SSSS – BSE.

From the SEM images of Z5 AS, figure 10 A & B, a clear structure of brighter features are visible on the darker background. The BSE image figure10 B confirms that these are microstructure features in the material. Since they are brighter, in Z contrast, they consist of heavier elements than the surrounding matrix. This aligns well with Zn having a higher atomic number than Mg. From the phase diagram, section 2.1 fig. 1, of the Mg-Zn system, it is reasonable to believe that these brighter features are precipitates of the eutectic Mg_7Zn_3 phase. The eutectic structure of the precipitates is confirmed at a higher magnification in figure 11. These precipitates are not visible in the SSSS samples, figure 10 C & D, confirming the microstructural state of the alloy. A slight grayscale contrast variation is visible in figure 10 D indicating local variations in the concentrations of alloying elements.

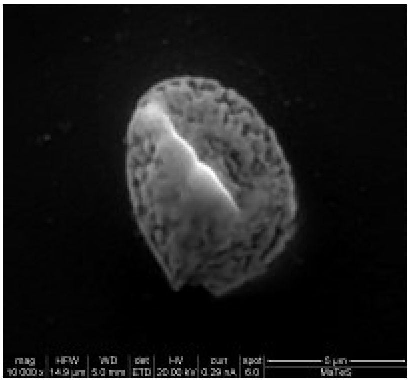

Figure 11: SE 10 000x magnification, of precipitate structure in Z5 AS.

This initial analysis confirms the expected microstructural states of the Z5 alloy samples; as-cast with precipitated eutectic phase and homogeneous super-saturated solid solution.

4.2 Isothermal calorimetry

The summary of isothermal calorimetry results is presented in figure 12 below. Raw data was analysed using the in-house python script, section 3.3.4. The corrosion rates and enthalpies are normalised versus surface area and presented in figure 12 with an average and statistical interval of 2 standard deviations (2σ).

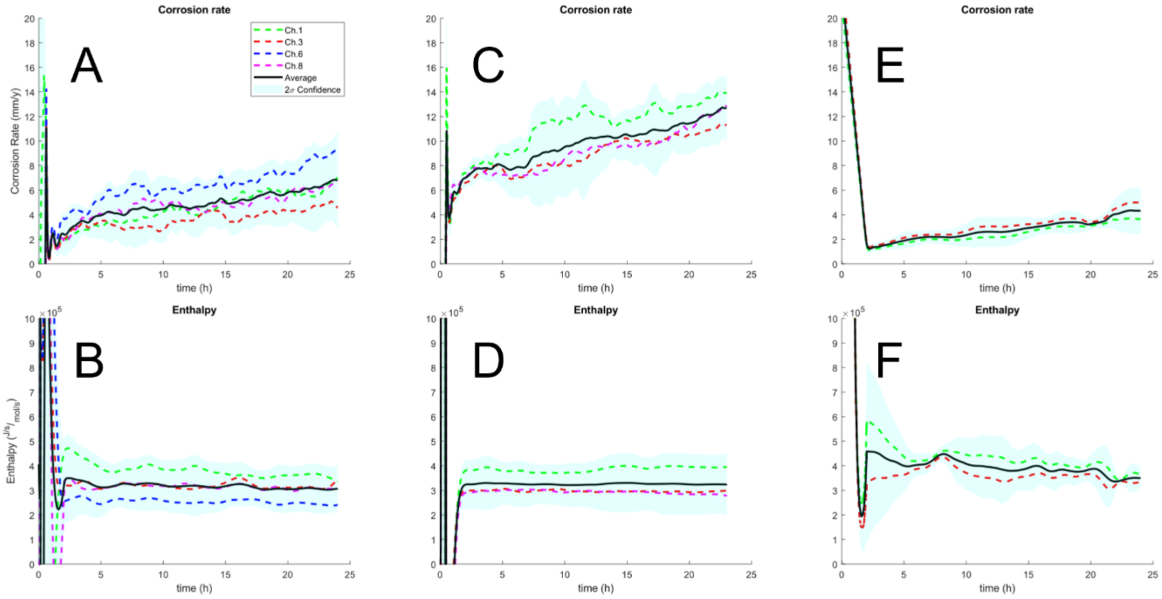

Figure 12: Corrosion rates; A, C & E (mm/year) and enthalpy variations; B, D & F for Z5 AS in A & B, Z5 SSSS in, C & D and ZX50 in E & F.

As can be seen in figure 12 above, Z5 AS report is based on all four specimens, Z5 SSSS on three specimens and ZX50 on two specimens. Channel 6 was excluded from the measurement of Z5 SSSS as it was considered an outlier due to a drop in pressure after 10 hours of measurement hinting at an insufficient sealing of the sample vial. Raw data of thermal power and pressure are presented in Appendix 1. Due to time constraints on the equipment, ZX50 was studied in parallel with other experiments, and hence only two chambers in the calorimeter were available resulting in only two specimens used. Since they present rather consistent results, they can be considered trustworthy.

All samples reached a steady increase in corrosion rate after 2 hours, see table 1 below. All three materials show, after the stabilization time of about 2 hours, a constant heat evolution responding to a constant enthalpy of the reactions. The corrosion rate (CR) & reaction enthalpy was averaged for the first and last hour after enthalpic stabilization which occurred after 2 hours. This was done to be able to compare the progress of reaction between materials.

Table 1: Corrosion rates (CR) of final hour of experiment, and reaction enthalpies (ΔH) from 3rd to final hour, of the studied materials.

Material	Corrosion rate, CR (mm/year)		Enthalpy, ΔH (kJ/mol)	
	1st stable hour	Last hour	1st stable hour	Last hour
Z5 AS (Mg-5.0Zn)	2.76 ± 0.28	6.71 ± 0.12	346 ± 6.52	304 ± 1.40
Z5 SSSS (Mg-5.0Zn)	7.40 ± 0.25	12.5 ± 0.16	325 ± 0.82	324 ± 0.14
ZX50 (Mg-5.0Zn-0.3Ca)	1.34 ± 0.065	4.33 ± 0.012	450 ± 6.40	350 ± 0.82

The recorded reaction enthalpies are similar to, but not matching the reaction enthalpies in section 2.2.1. This suggests that side reactions occur in the setup.

The difference from expected reaction enthalpies, -353 kJ/mol, may be explained by the domination of different reaction steps within the system. From reaction (2) and (3) in section 2.2.1 we see that a suggested reaction path is to first oxidate Mg and then in a consecutive reaction hydroxylate MgO. If there are any hindrances of these to reactions, such as evolution of pH in the system, one of the reactions would dominate. This has been studied in previous work (Viklund 2020) where it was shown that a similar system saturates in pH after 4 hours. A increase in pH stems from an increasing [OH^-], which is one of the dissolving products of $Mg(OH)_2$. Hence a saturation in pH would impede the hydroxylation reaction, explaining why Z5 AS shows a steady state, 318 kJ/mol much closer to the reaction enthalpy of the oxidizing step, 315 kJ/mol, than the sum of oxidation and hydroxylation, 353 kJ/mol.

4.2.4 Comparison of results

To compare the results of degradation rates with published degradation rates, multiple publications were studied, and the following comparison table is produced.

Table 2: Comparison of corrosion studies of Mg-Zn & Mg-Zn-Ca alloys with low alloying contents.

Composition	**Condition**	**Electrolyte**	**Temp.** (°C)	**Method**	**Corrosion rate** (mm/y)	**YS** (MPa)	**UTS** (MPa)	**Reference**
Mg (99.9 %)		c-SBF	37	Gravimetric	6.2		197	Guan et al., (2013)
Mg-0.5Zn	AS	SBF	37	CCD	3.1	75	112	Koç et al., (2015)
Mg-0.5Zn	AS	SBF	RT	CCD / H2 evol.	1.2 / 1	38	95	Peng et al., (2012)
Mg-0.5Zn	Backward-extrusion	SBF	RT	CCD / H2 evol.	0.5 / 0.5	62	145	Peng et al., (2012)
Mg-1.25Zn	AS	SBF	37	CCD / Gravimetric	6.5 / 3.2			Bakhsheshi-Rad, et al., (2014)
Mg-1.5Zn	AS	SBF	RT	CCD / H2 evol.	8.5 / 1.4	51	109	Peng et al., (2012)
Mg-1.5Zn	Backward-extrusion	SBF	RT	CCD / H2 evol.	1.3 / 0.5	101	190	Peng et al., (2012)
Mg-1Zn	AS	SBF	37	CCD	2.8	80	128	Koç, et al., (2015)
Mg-1Zn	AS	0.9 *wt. %* NaCl		CCD / Gravimetric	0.9 / 1.3			Kubasek, et al., (2013)
Mg-1Zn	Backward-extrusion	SBF	37	CCD / H2 evol.	1.1 / 0.5	91	169	Peng et al., (2012)
Mg-1Zn	AS	SBF	RT	CCD / H2 evol.	4.1 / 1.1	43	99	Peng et al., (2012)
Mg-2.5Zn	AS	SBF	37	CCD / Gravimetric	5.5 / 2.4			Bakhsheshi-Rad, et al., (2014)
Mg-2Zn	Extrusion	0.6 M NaCl		Gravimetric	3.4			Ha et al., (2013)
Mg-2Zn	AS	SBF	37	CCD	2.6	86	137	Koç et al., (2015)
Mg-2Zn	AS	SBF	RT	CCD / H2 evol.	9.7 / 1.3	65	121	Peng et al., (2012)
Mg-2Zn	Backward-extrusion	SBF	RT	CCD / H2 evol.	1.4 / 0.6	111	198	Peng et al., (2012)
Mg-2Zn	Extrusion	3.5 *wt. %* NaCl		CCD	0.2			Song et al., (2012)
Mg-2.65Zn	AS	0.9 *wt. %* NaCl		Gravimetric	13.4	45	145	Zheng et al., (2015)

Composition	**Condition**	**Electrolyte**	**Temp.** (°C)	**Method**	**Corrosion rate** (mm/y)	**YS** (MPa)	**UTS** (MPa)	**Reference**
Mg-3Zn	AS	SBF	37	CCD / Gravimetric	5.2 / 2			Bakhsheshi-Rad et al., (2014)
Mg-3Zn	AS	MEM	37	H2 evol.	0.5			Chen et al., (2012)
Mg-3Zn	Extrusion	0.6 M NaCl		Gravimetric	8.4			Ha et al., (2013)
Mg-3Zn	AS	SBF	37	CCD	2.3	93	147	Koç et al., (2015)
Mg-3Zn	AS	9 g/L NaCl		CCD / Gravimetric	0.9 / 2.5			Kubasek et al., (2013)
Mg-3Zn	AS	0.1 M NaCl		CCD / H2 evol.	0.5 / 1.5			Liu et al., (2010)
Mg-3Zn	Bi-directional Rolling	SBF	37	CCD / Gravimetric	2.6 / 2	49	183	Nayak et al., (2016)
Mg-3Zn	Extrusion	3.5 *wt. %* NaCl		CCD	0.3			Song et al., (2012)
Mg-4Zn	AS	SBF	37	CCD / Gravimetric	4.9 / 2.1			Bakhsheshi-Rad, et al., (2014)
Mg-4Zn	Extrusion	0.6 M NaCl		Gravimetric	10			Ha et al., (2013)
Mg-4Zn	Extrusion	3.5 *wt. %* NaCl		CCD	0.4			Song et al., (2012)
Mg-5.0Zn	AS	0.9 *wt. %* NaCl	37	H2 evol.	4.8			Reinwalt & Tayeb-Bey (2019)
Mg-5.0Zn	AS	m-SBF	37	H2 evol.	0.8			Viklund (2020)
Mg-5.0Zn	Solid solution treatment	m-SBF	37	H2 evol.	0.5			Viklund (2020)
Mg-5.0Zn	AS	0.9 *wt. %* NaCl	37	H2 evol.	6			Viklund (2020)
Mg-5Zn	AS	SBF	37	CCD / Gravimetric	0.3 / 1.3	76	195	Cai et al., (2012)
Mg-5Zn	Solid Solution Treatment	3.5 *wt. %* NaCl		CCD / H2 evol. / Gravimetric	2.7 / 10 / 6.5			Cao et al., (2013)
Mg-5Zn	Extrusion	3.5 *wt. %* NaCl		CCD	0.5			Song et al., (2012)
Mg-5Zn	AS	3.5 *wt. %* NaCl		CCD / Gravimetric	0.6 / 2.7			Song et al., (2012)
Mg-5Zn	T4	3.5 *wt. %* NaCl		CCD / Gravimetric	0.5 / 2.3			Song et al., (2012)
Mg-5Zn	T6 (4 h ageing)	3.5 *wt. %* NaCl		CCD / Gravimetric	1.2 / 4			Song et al., (2012)

Composition	**Condition**	**Electrolyte**	**Temp.** (°C)	**Method**	**Corrosion rate** (mm/y)	**YS** (MPa)	**UTS** (MPa)	**Reference**
Mg-5Zn	T6 (10 h ageing)	3.5 *wt. %* NaCl		CCD / Gravimetric	1.5 / 5.5			Song et al., (2012)
Mg-5Zn (ultrapure)		3.5 *wt. %* NaCl, $MgOH_2$ saturated	25	H2 evol. / Gravimetric	1 / 1.8			Shi et al., (2015)
Mg-5Zn (ultrapure)		3.5 *wt. %* NaCl, $MgOH_2$ saturated	25	H2 evol. / Gravimetric	2.3 / 3.4			Shi et al., (2015)
Mg-6Zn	AS	SBF	37	CCD / Gravimetric	6.2 / 3.5			Bakhsheshi-Rad et al., (2014)
Mg-6Zn	Extrusion (PM)	Ringer's	37	CCD	0.4			Yan et al., (2017)
Mg-6Zn	AS					69	182	Zhang et al., (2011)
Mg-6Zn	Extrusion	SBF	37	CCD / Gravimetric	0.16 / 0.07	170	280	Zhang et al., (2010)
Mg-6Zn	Extrusion	*in vivo*		Gravimetric	2.3			Zhang et al., (2010)
Mg-6Zn	Extrusion	SBF	37	CCD / Gravimetric	5.4 / 12.6			Zhang et al., (2016)
Mg-7Zn	AS	SBF	37	CCD / H2 evol.	1.2 / 3.2	67	136	Cai et al., (2012)
Mg-0.8Zn-0.6Ca	AS	HBSS	37	CCD / Gravimetric	0.08 / 0.1			Zander & Zumdick (2015)
Mg-0.8Zn-0.6Ca	AS	PBS	37	CCD / Gravimetric	0.02 / 0.1			Zander & Zumdick (2015)
Mg-1.2Zn-0.5Ca	AS	SBF	37	CCD / Gravimetric	15.8 / 8.2	60	121	Ibrahim et al., (2017)
Mg-1.2Zn-0.5Ca	T6	SBF	37	CCD / Gravimetric	9.6 / 4.8	84	151	Ibrahim et al., (2017)
Mg-1Zn-0.5Ca	Extrusion					105	210	Zhang et al., (2012)
Mg-0.8Zn-1.6Ca	AS	HBSS	37	CCD / Gravimetric	0.1 / 0.2			Zander & Zumdick (2015)
Mg-0.8Zn-1.6Ca	AS	PBS	37	CCD / Gravimetric	0.04 / 0.2			Zander & Zumdick (2015)
Mg-1.8Zn-0.6Ca	AS	HBSS	37	CCD / Gravimetric	0.03 / 0.1			Zander & Zumdick (2015)

Composition	**Condition**	**Electrolyte**	**Temp.** (°C)	**Method**	**Corrosion rate** (mm/y)	**YS** (MPa)	**UTS** (MPa)	**Reference**
Mg-1.8Zn-0.6Ca	AS	PBS	37	CCD / Gravimetric	0.02 / 0.2			Zander & Zumdick (2015)
Mg-1Zn-1Ca	AS	Hank's	37	Gravimetric	2.1	45	125	Zhang & Hou et al., (2011)
Mg-2Zn-0.24Ca	AS	SBF	37	CCD	12.1			Gao et al., (2011)
Mg-2Zn-0.24Ca	HPT	SBF	37	CCD	0.08			Gao et al., (2011)
Mg-2Zn-1Ca	AS	Hank's	37	Gravimetric	2.4	52	143	Zhang & Hou et al., (2011)
Mg-1.8Zn-1.6Ca	AS	HBSS	37	CCD / Gravimetric	0.04 / 0.2			Zander & Zumdick (2015)
Mg-1.8Zn-1.6Ca	AS	PBS	37	CCD / Gravimetric	0.06 / 0.3			Zander & Zumdick (2015)
Mg-3Zn-0.2Ca	Extrusion	SBF	37	Gravimetric	1.2	224	273	Li et al., (2016)
Mg-3Zn-0.3Ca	AS	SBF	37	H2 evol.	6.9			Lu et al., (2015)
Mg-4Zn-0.2Ca	Extrusion	SBF	37	Gravimetric	1.3	243	295	Li et al., (2016)
Mg-4Zn-0.5Ca	AS	Hank's	37			70	180	Zhang et al., (2011)
Mg-4Zn-1Ca	AS	Hank's	37	Gravimetric	4.4	63	182	Zhang & Hou et al., (2011)
Mg-5Zn-0.27Ca	AS	0.9 *wt. %* NaCl	37	H2 evol.	2			Viklund (2020)
Mg-5Zn-0.27Ca	AS	m-SBF	37	H2 evol.	2.7			Viklund (2020)
Mg-5Zn-0.27Ca	Heat treated 450 °C 24h	m-SBF	37	H2 evol.	1.5			Viklund (2020)
Mg-5Zn-1Ca	AS	Hank's	37	Gravimetric	6.2	65	173	Zhang & Hou et al., (2011)
Mg-6Zn-1Ca	AS	Hank's	37	Gravimetric	9.2	67	145	Zhang & Hou et al., (2011)

The corrosion rates measured in this study are consistent and align within the ranges of previous documented data from the literature. It is worth noting the spread on corrosion rates with the use of different measuring methods and corrosive media as well as significant variation of SBF composition between publications.

4.3 DCT

An overview of the full absorption contrast volume of the studied materials is presented in figure 13 below.

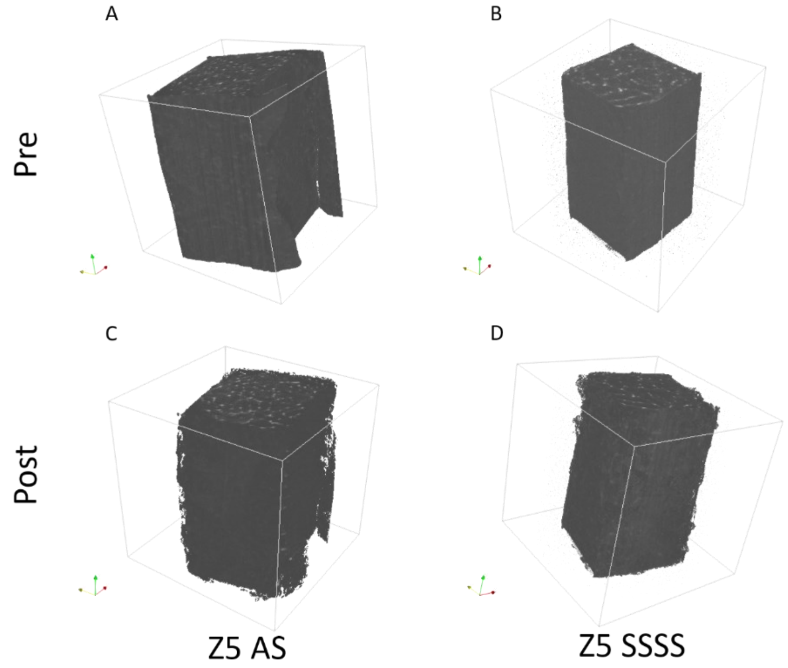

Figure 13: DCT Absorption contrast of: A: Z5 AS Pre exposure to electrolyte, B: Z5 SSSS Pre exposure to electrolyte, C: Z5 AS post 24h exposure to electrolyte & D: Z5 SSSS post 24h exposure to electrolyte.

During immersions between the DCT measurements, a build-up of rust on the sample holder was observed after the first immersion test. To prevent this during the second immersion test, the sample holder was wrapped in plastic, but some rust was still observed on the sample holder after immersion. To further prevent this, the sample was mounted on a plastic stick in the following experiments, so that the vice of the sample holder would reside outside the vial during immersion.

The steps in improving sample holding are illustrated in figure 14 below.

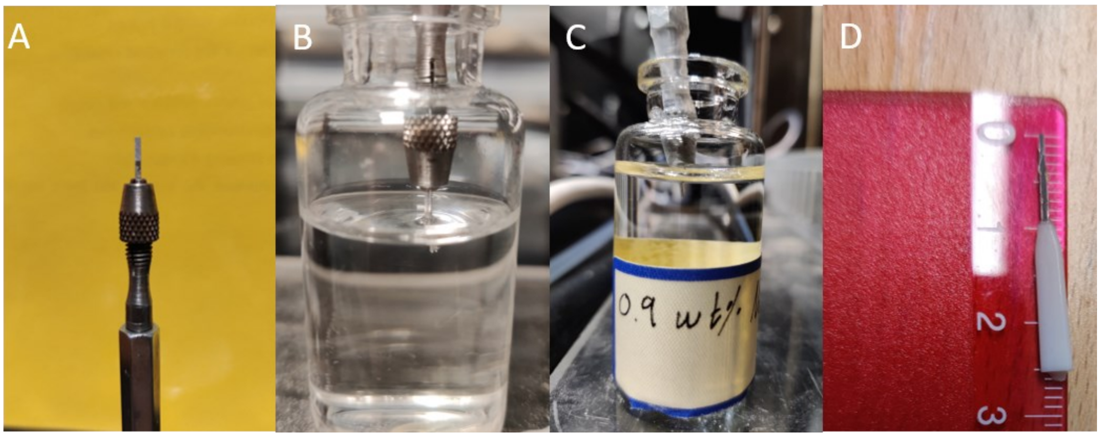

Figure 14: Evolution of protection for sample holder in DCT experiments. A: sample in sample holder vice. B: First immersion setup. C: Second immersion setup – holder wrapped in plastic film. D: Sample mounted on plastic stick for final immersion setup.

The minor corrosion and the protection of the vice had no detectable effect on scan quality and was only used to protect the tool, hence all scans were useable independent of sample mounting design. It is believed that the rust stems from the saline vapour rising from the electrolyte and not dispersing below the neck of the vial. Furthermore, since no electrolyte was present where the sample holder is in contact with the sample, and the studied area was close to the tip of the sample, it is believed that no galvanic coupling between sample and sample holder interfered with the measurements.

Representative slices (Z axis) of the absorption contrast from the DCT scans are presented for each material sample in figure 15 below. Across all samples, a predominately homogeneous corrosion can be observed by comparing cross-sections of the same samples before and after the exposure. This is exemplified with a representative selection in figure 15 below. Here a local corrosion spot can be observed in D, highlighted by the green circle. These spots will be the centre of analysis of the DCT section as corrosion affects the sample more severely in these spots, compared to the rest of the surface where more homogeneous corrosion was observed, as seen in figure 15 B. The criterion for identification of such a spot was defined as having a mouth (D1) and depth (D2) equal or larger than 50 µm.

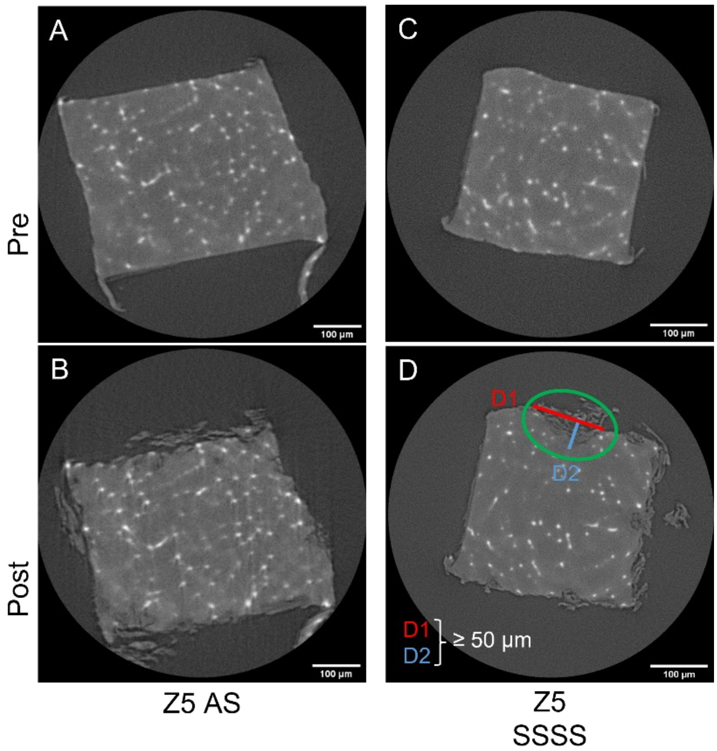

Figure 15: DCT absorption contrast of studied samples cross-section slices in Z plane. Localized corrosion in Z5 SSSS marked in green circles. Distance across localized corrosion marked in red and blue as D1 & D2.

To analyse these spots, the reconstruction from the diffraction patterns obtained were overlaid with the absorption contrast to visualise crystallographic orientations around the location of the corrosion attack. The distances across the surface and the depth where localized corrosion occurs were measured, as highlighted in figure 15 D above. 5 of these localized corrosion instances were discovered per sample. Careful analysis of these 10 localized corrosion events suggests that the localized corrosion spots are always encompassed or limited by the intermetallic particles. The size of spots on the specimen surface is defined as the distance between the spot-limiting precipitates. The criterion for localized corrosion is a depth and width above 50 µm, visualised in figure 15. The grains attacked by corrosion are summarized in an inversed pole figure (IPF) in section 4.3.4.

For each corrosion spot found two images are produced, see figure 16 & figure 17, one in Z plane and one in the facial plane of corrosion instance. The analysed images were horizontal and vertical cuts.
The reconstructions show circular patterns close to the limits of the scanned volume in Z direction. These are believed to be reconstruction artifacts, and localized corrosion instances within this volume were ignored.

4.3.1 Z5 AS

An overview of the absorption contrast was presented in figure 13.

The reconstruction of Z5 AS was performed with a voxel size of 4 µm, 205 identifiable grains with a size larger than 10 voxels were identified. Most of the identifiable grains were small and only a handful are visible and relevant for the analysis.

As is represented in figure 15 B The sample did undergo homogeneous corrosion around its surface, except for the identified localized spots. The resolution of the images does not allow for deeper analysis of this homogeneous corrosion.

The sample was exposed 24 hours to the electrolyte. From the reconstruction and absorption contrasts, it was possible to identify five spots of localised corrosion. The localised corrosion occurs on three different grains of which two grains have two instances of corrosion on two different faces. The localised corrosion spots are presented in figure 16 and the orientation of the attacked grains are presented in the inverse pole figure (IPF) in figure 17.

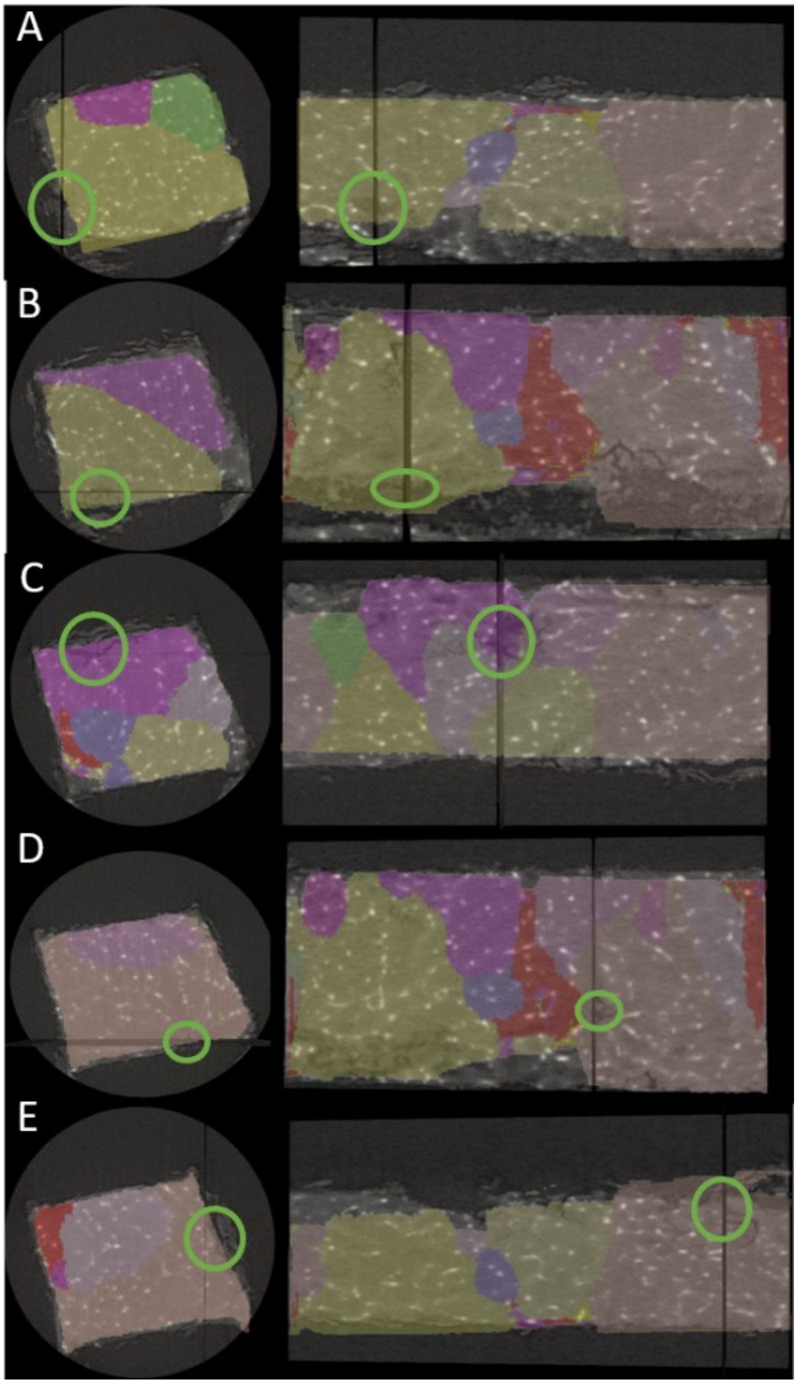

Figure 16: Identified localized corrosion spots in Z5 AS sample. DCT absorption with overlaid grain structure from DCT diffraction. Coloration of grains in 0001 reference direction. Lines in reference to where the coupled image resides within the sample volume.

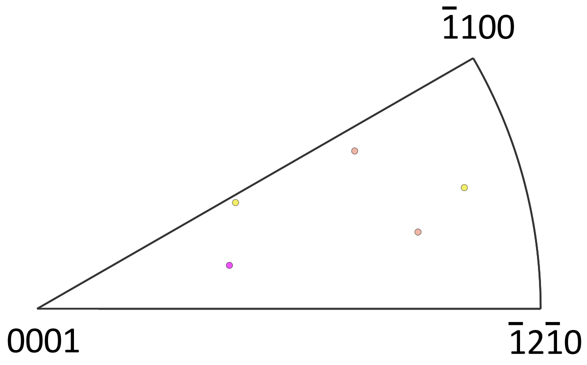

Figure 17: Inverse Pole Figure showing orientations of grains in Z5 AS where localized corrosion occurred. Coloration of dots in reference to (0001) IPF.

It can be observed that all localised corrosion occurs in the grain interiors in a matrix area surrounded by the intermetallic precipitates. Such regions with localised corrosion extend into the bulk of the sample for all spots.

4.3.2 Z5 SSSS

An overview of the absorption contrast was presented in figure 13.

The reconstruction was performed following the same procedure as for Z5 AS, with a voxel size of 4 µm, 22 grains larger than 10 voxels were identified. Most of the grains identified were small grains with two grains dominating the volume of the sample.

The absorption contrast scans in figure 13 (C&D) and figure 15 (C&D) show precipitates in the material, which contradicts the results of SEM examination, figure 10 c, d. This can be explained by significantly larger volume of the material examined in X-ray tomography on the background of incomplete solid-solutioning, which was not detected in SEM examination. The count of precipitated particles is however lower for the SSSS state than the AS state, visible later in figure 23.

Five instances of localized corrosion were observed in this sample, as shown in figure 18 below.

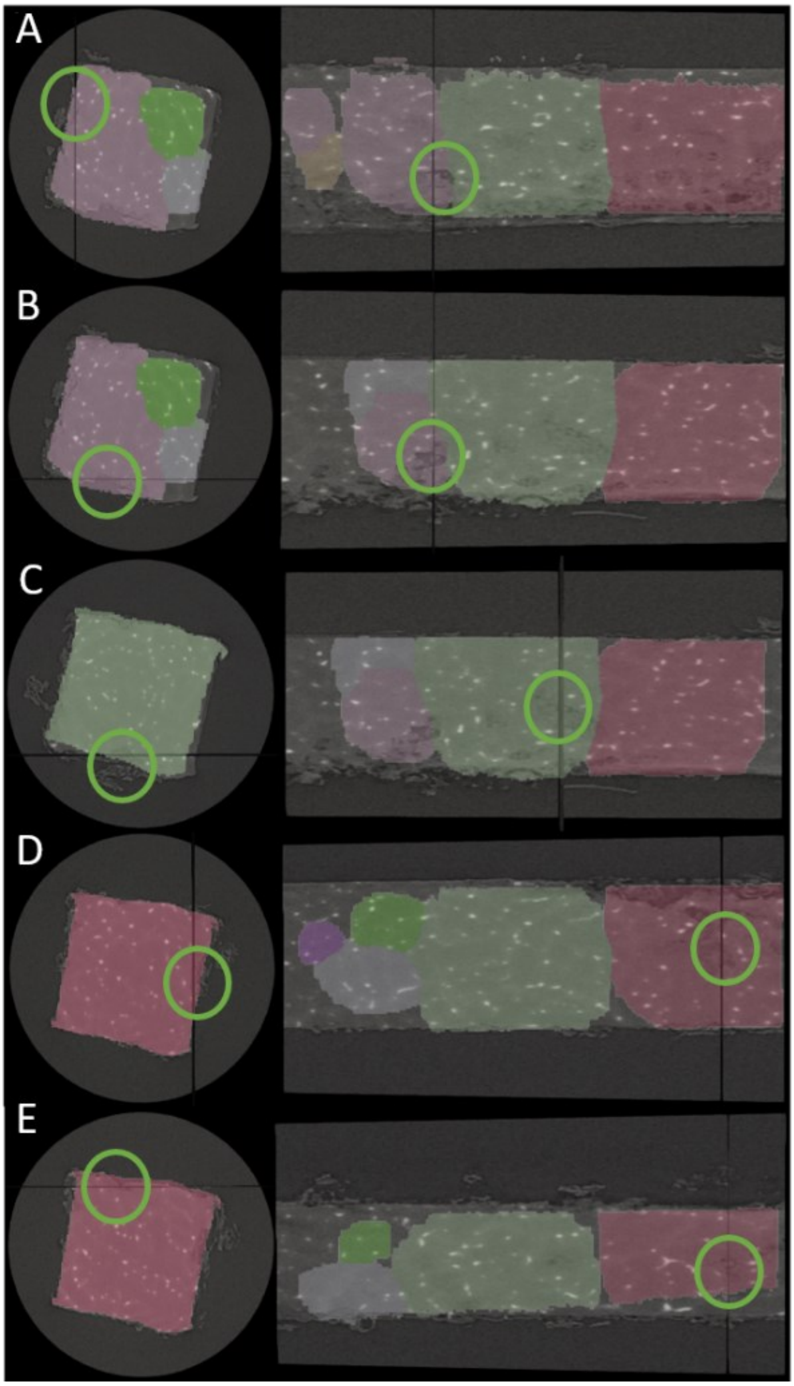

Figure 18: Identified localized corrosion Z5 SSSS. DCT absorption with overlaid grain structure from DCT diffraction. Coloration of grains in 0001 reference direction.

Worth noting is that the grain structure of this material consists of three larger grains in, the remaining 19 identified grains are smaller and found in not relevant areas for the analysis.

The orientation of the attacked grains are presented in the inverse pole figure (IPF) in figure 19.

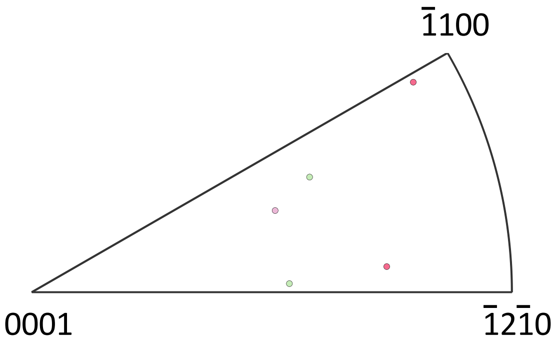

Figure 19: Inverse Pole Figure showing orientations of grains in Z5 SSSS where localized corrosion occurred. Coloration of dots in reference to (0001).

4.3.4 Summarizing DCT

All the material samples show predominantly homogeneous corrosion with a few localized corrosion spots in certain areas. The orientation of interfaces that were subjected to localized corrosion is summarized in the combined IPF below, figure 20. Gridlines were added to easier be able to read the angle of misorientation for the orientations in focus.

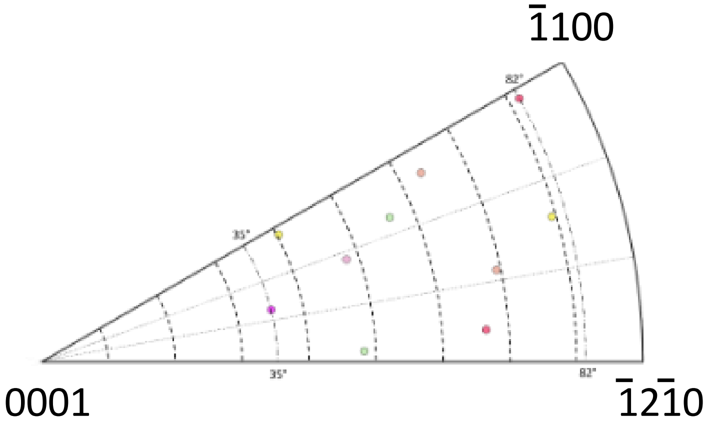

Figure 20: Combined IPF of both Z5 materials of grains that exhibited localized corrosion. Gridlines represent 10° rotations. Closest and furthest rotation from (0001) marked.

In the most cases of all studied materials, localized corrosion spots are initiated in the areas of solid-solution matrix far from precipitate particles. These areas are in all instances surrounded by precipitates in a pattern at a rather constant distance between each other. This is representatively presented in figure 21, and further analysed in section 5.1.

The distances across the surface where the localized corrosion spots are seen is summarized in table 3 below. The third measurement, 314 µm, of Z5 AS , figure 16 C, is considered an outlier and hence excluded from calculating the average distance.

Table 3: Specific and averaged distances across identified localized corrosion instances summarized per material.

Material	D (µm)	D/2 (µm)	Avg. D (µm)
Z5 AS	55	27.5	126 ± 55
	150	75	
	116	58	
	184	92	
Z5 SSSS	148	74	120 ± 25
	90	45	
	143	71.5	
	115	67.5	
	103	51.5	

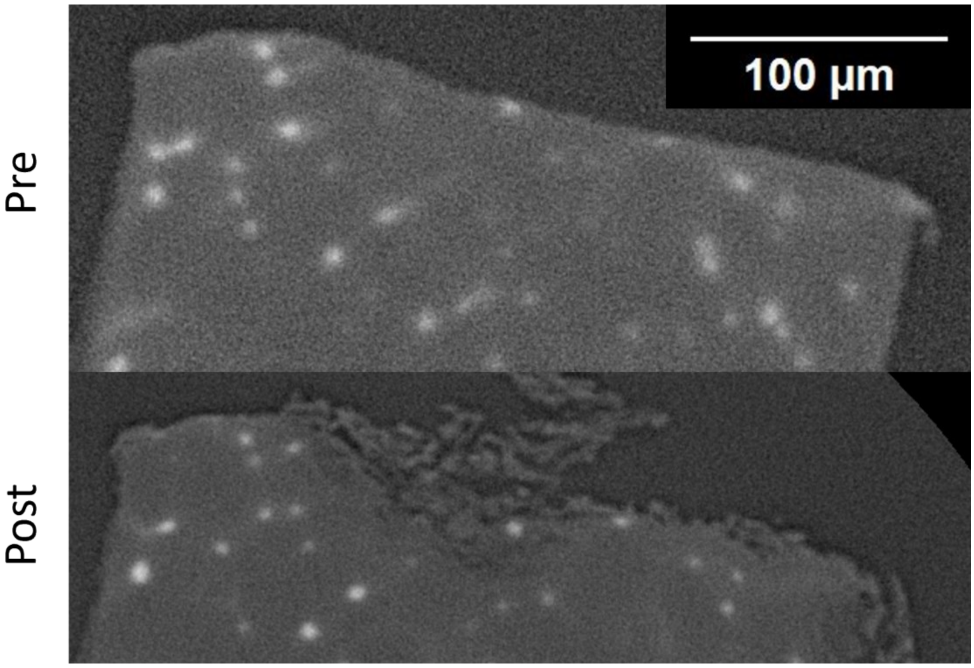

Figure 21:Z5 AS localized corrosion spot C. Top, Pre exposure, Bottom post exposure.

As can be seen in figure 21, the arc of removed material stretches between precipitated particles. The central particle (pre- exposure) has been undermined and drifted into the corroded volume. Each precipitated particle close to the corroded area also is enclosed by the continuous material.

5. Analysis and Discussion

5.1 Dependence of average degradation on material microstructure

By carefully analysing the areas where localized corrosion occurs, it can be found that the propagation of corrosion is suppressed by a network of non-dissolved precipitates. The precipitates are of eutectic composition, as confirmed by the SEM analysis, figure 11. By Z-contrast, these precipitates must contain more Zn than the matrix material making them more noble than the matrix. A more noble particles would act as a micro-cathode, and the magnesium matrix with relatively lower Zn-concentration and hence lower electronegativity will then acts as a micro-anode. The anode is preferentially corroded according to the half-cell reaction (Song, 2011). It can be observed in the absorption contrast from the DCT data, Figure 21, that the secondary phase precipitates is encompassed by primary phase after exposure.
The precipitate network is believed to fill two roles.

First, the network of precipitate structure accelerates localised corrosion through the suggested galvanic coupling. In certain locations, two or more intermetallic particles may have an accelerating effect when separated by a specific distance from each other. At such a distance, corrosion would accelerate due to two micro-galvanic cells acting upon the same volume of material, increasing the rate of ion depletion from that site. The suggested process is illustrated in figure 23 below.

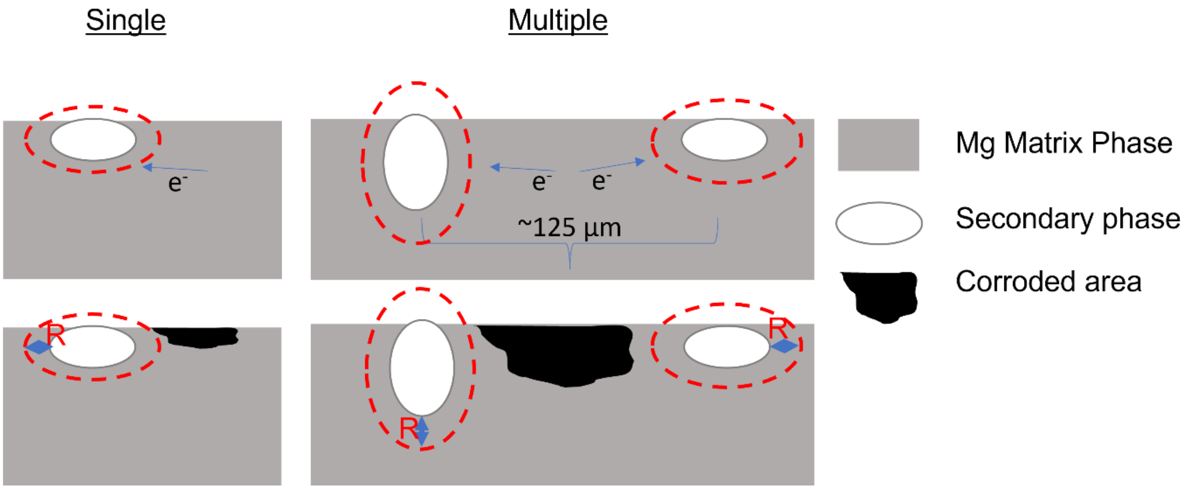

Figure 22: Sketch of suggested electrochemical protection around precipitates. The more noble precipitates, white ellipsoids, carry a gradient in electronegativity towards the less noble matrix, red ellipsoids, over a radius R.

In figure 22 above, the corrosion process has been simplified to the motion of electrons, counter-ions ($Mg^{+/2+}$) are dissolved in the surrounding solution immediately, the exact reaction path is still under research (Mei et. al., 2020). This gradient of electronegativity is believed to be the reason why areas with a certain, by measurements approximately 125 µm, distance of precipitates from the centre shows different corrosion behaviour than other areas.

Second, since the intermetallic phases show a lower corrosion rate than the matrix, they are also believed to act as barriers suppressing the corrosion process in a volume around themselves, illustrated as R in figure 22. In the publication by Song (2011) similar explanation is given based on AZ alloys and speculated to be applicable also to other similar alloys. This principle seems to work for the alloys studied in current work, visualised in figure 21.
Following this reasoning, a material with more precipitates would corrode slower due to a larger

passivated volume around each precipitate is present. This is observed in the results of the calorimetric tests, as Z5 AS shows a lower corrosion rate than Z5 SSSS, see table 1.

From the DCT absorption scans, figures 15 (c, d) and figure 18, it is visible that precipitates are present in the SSSS material hinting that the material has aged in its stored conditions, somewhat reversing the solid solution treatment However, since the precipitate count is visibly lower, see figure 24, and grains are larger than in the AS state, the reasoning on precipitate involvement in degradation process and rate still stands.

In the calorimetric measurements, an initial minimum observed for all materials and specimens is believed to be mainly due to the loss of heat upon sample loading into the vial, as the vial has to be removed from the thermostatic environment. To minimise these effects, the procedure when loading specimens was mimicked as close as possible to the procedure of mounting vials for the baseline recording.

It is plausible that the corrosion rate is initially higher, hidden during the thermal lag of loading specimens, since the corrosion reaction is a surface reaction that forms semi-protective films of corrosion products on the surface of the sample. When the sample is introduced to the electrolyte, no such film exits, and a clean material surface is exposed. At the same time, it is well known that in gaseous environment (air) a relatively stable MgO film forms on Mg surface, while in wet and aqueous environment $Mg(OH)_2$ film is more stable (Viklund 2020) . In comparison to when the corrosion film has formed, less electrolyte would reach the surface of the sample where the corrosion reactions take place hence lowering the corrosion rates. The formation and structure of the protective layers are further discussed in Viklund (2020). The initial non-equilibrium state may also affect the rate of corrosion depending on the order of reaction. Since the system is complex and many reactions occur simultaneously, no definitive answer may be given based on this study alone. The recorded enthalpy values are close but do not exactly match theoretically calculated enthalpies for the degradation reactions. This indicates that side reactions, unaccounted for in section 2.2.1, do occur in the system. However, since the corrosion rates are calculated from the release of hydrogen gas, equation (E2), the reported corrosion rates are unaffected, assuming no side reaction consuming any gaseous constituent is occurring in the system.

One error source worth considering is the orientation of the samples during calorimetric measurements in contrast to where the corrosion product ends up. The specimens were oriented so that the largest surface was horizontal, visible in figure 7 C. Any corrosion products formed on this surface facing upwards will not fall off, compared to the same surface on the bottom side of the sample. In a publication by (Maier, P. et al., (2019)) a similar phenomenon can be observed, where the samples corrode differently on the different surfaces, depending on the build-up or fall-off of corrosion products. In referenced work the difference in corrosion behaviour depending on the orientation of the sample was commented as not interfering with the reported results.

5.2 Dependence of degradation on crystallographic orientation

For both microstructural states of the Z5 material, all localized corrosion occurs within single grains. To study the orientation of the attacked grains, a combined IPF from both microstructural states was produced, figure 20. The orientation of grains was observed to deviate from the three low-index planes, (0001) $(11\bar{2}0)$ and $(10\bar{1}0)$.As shown in figure 20, no localized corrosion occurred neither on nor close to the (0001) plane. The closest rotation from (0001) is at a 35° misorientation. The (0001) plane is present in the studied material as can be seen in figure 16. It is believed that the reason this plane does not exhibit localized corrosion is due to the atomic packing density of the (0001) plane is the highest of the low index planes in magnesium, (Song, 2011). Comparing the atomic packing density (APD) of the three low index planes of the HCP structure, (0001) $(11\bar{2}0)$ and $(10\bar{1}0)$, is 1.13 x 10^{15}, 6.94 x 10^{14} and 5.99 x 10^{14} atoms/cm^2 respectively. The planes parallel to the c-axis, $(hki0)$ planes, has lower atomic packing density compared to the (0001) plane. Higher index planes will have lower APD and hence only the low index planes are discussed. A plane with more atoms per unit area must have shorter, and therefore stronger, atomic bonds. In other words, higher atomic coordination is coupled with larger atomic binding energies. The interfacial energy, or surface energy, must then scale inversely to the atomic density in the surface planes. Dissolution, which is theorised to be a participating step in the corrosion of magnesium, should then be less favoured on surfaces with larger binding energies, (Liu et al., 2008). Higher-index planes will have a lower APD, and hence only the three low index planes are used as examples. In figure 20, it is highlighted that localized corrosion occurs in planes with rotations 35° - 82° off (0001). This offset matches the present discussion. Notably there is also a larger offset from the $(11\bar{2}0)$ pole compared to the offset from the $(10\bar{1}0)$ pole, which also in line with the present discussion. However, the offset is smaller as the APD is more similar in these planes. This discussion matches with packing density only in rotations from (0001), however the difference in offset from $(11\bar{2}0)$ and $(10\bar{1}0)$ is seemingly larger in comparison to the difference in APD.

It may be speculated that the offset from each pole in the IPF corresponds to planes with similar APD. More thorough investigation into this is needed but is out of scope for current work.

It should be noted that only 10 instances of localized corrosion were observed in the presented study. Although they demonstrate the trend, a larger sample size with better statistical representation would be necessary for confirming the trend. In fact, a larger dataset has been collected already in collaboration with Xnovotech™, but its detailed analysis is beyond the scope of current work and is planned for a follow-up study.

It would also be useful in this work to determine degradation rates by the loss of material from the segmentation of absorption contrast in DCT data, which would require the separation of corrosion products from the bulk material. In the absorption contrast, corrosion products could not be segmented from bulk material by binning intensity signals. This is because variations in intensity are very similar for bulk sample as for what could be assumed to be corrosion product on the surface of the sample. As absorption contrast depends on atomic number, and magnesium is the main component in both bulk material and corrosion product, it is understandable that the segmentation is difficult. As a result, when segmenting the dataset, the bulk material in the centre of the sample is removed in segmentation at the same time as what is believed to be corrosion product. To be able to perform such an analysis, a more advanced segmentation methods are necessary.

5.3 Comparison of results with literature data and further implications

The discussion in 5.2 on APD and surface energies is consistent with earlier report by Song, Mishra & Xu (2010) where difference in electrochemical dissolution rates as a function of crystallographic planes is evaluated. They conclude that the theoretical dissolution rate should be 18- 20 times higher for $(10\bar{1}0)$ and $(11\bar{2}0)$ compared to (0001). Such a conclusion agrees, as a binary, with present findings as no corrosion were observed at (0001) surface.

Based on the previous discussion, the dominant feature driving the occurrences of localized corrosion is the spread and distances between precipitates coupled with the misorientation of at least 35° from the basal plane. To further investigate and understand this, a model to simulate electrochemical potential of the precipitates must be built and compared with a segmented mesh structure of the precipitates. Such a mesh structure can be easily obtained from the acquired absorption contrast in the DCT measurements, see figure 24 below. This might shine some light on the process of potential galvanic coupling of singular precipitate particles, as described by Song (2011) & Esmaily et al. (2017).

The lower concentration of precipitated particles in the SSSS alloy would by previous reasoning provide less protection from electrochemical reactions compared to the AS alloy. This reasoning is supported by the difference in corrosion rates discovered by the calorimetric measurements. The Z5 SSSS alloy corrodes faster than the Z5 AS alloy.

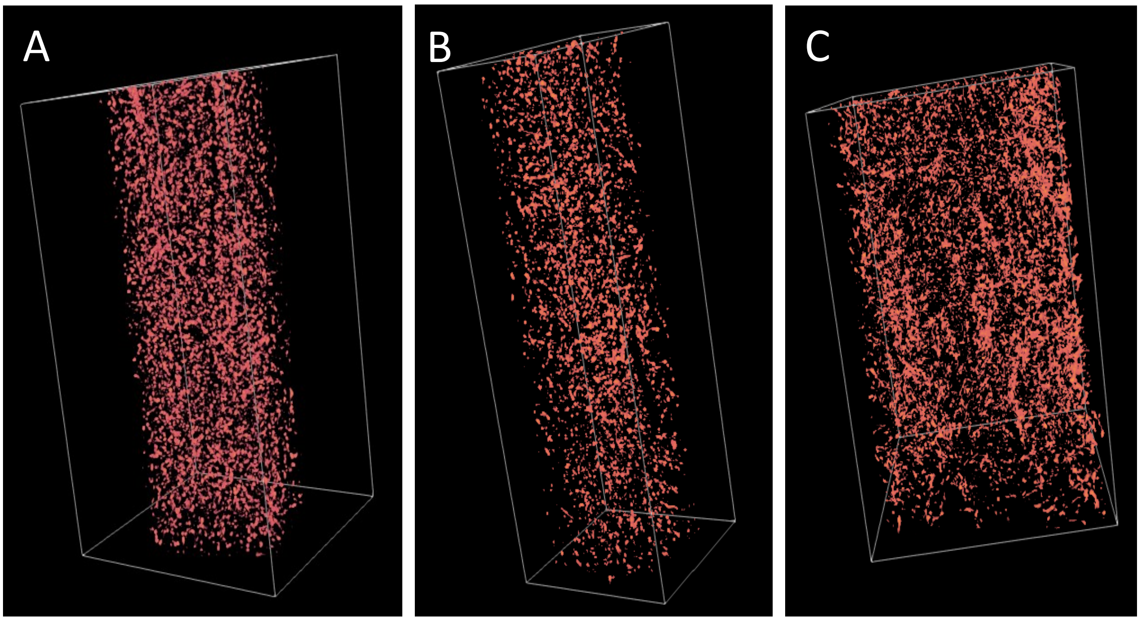

Figure 23: Segmented precipitate particles in DCT data. A: Z5 AS, B: Z5 SSSS & C: ZX50 alloys

Other studies, e.g., by Zhao, Y., et al., (2022), where DCT with immersion is used to analyse the degradation of Al 6061 alloy, show similar corrosion behaviour with localized pits forming. However, one notable difference stands out. This report states that corrosion on grain boundaries occurs later than corrosion on grain interfaces in the studied alloy. In comparison to current work, where corrosion was only observed on grain interiors, it might suggest that the immersion times are not long enough for intergranular corrosion to be resolved. Otherwise, differences can be attributed to the totally different corrosion behaviour in the Al 6061 alloy system.

Conclusions

Concluding this work, a few main points can be stated.

Corrosion rates of the studied materials were measured by hydrogen evolution and the reported corrosion rates falls within previous reported findings. The recorded enthalpies for the corrosion reactions suggests that with the setup used, the oxidation reaction of Mg to MgO seems to be dominant for both Z5 materials while both oxidation and hydroxylation occurs for ZX50.

From DCT studies an even corrosion across the surface of the samples were observed, except for certain locations. These locations all occurred within areas enclosed by precipitated particles. The precipitated particles in these locations were situated within a narrow spread with an approximate distance of 125 µm. All these instances were observed at grains with a misorientation between 35-82° from the (0001) plane. The reason for this misorientation is believed to be a consequence of atomic packing density of the exposed faces.

The degradation process is believed to be driven by the galvanic current occurring between the more noble precipitates and the less noble continuous phase.

Future Work and improvements

The data gathered in this work invites further analysis.

The analysis performed would, as mentioned in section 5.2, benefit from a larger dataset as only 5 instances of localized corrosion were observed in each material. To be able to handle larger datasets, an automated method for identification of localized corrosion and analysis would be needed.

Since the degradation occurs on the surface of the sample with some preference to interfaces which showed localized corrosion, see section 5.2. Analysis of how epitaxial growth of corrosion product (MgO) on a terraced surface that showed corrosion would be of interest to better understand the build-up and breaking of the corrosion product layers on the material. This could be studied by calculating lattice strains occurring from lattice mismatches. The process of oxidizing magnesium has been probed by using environmental transmission electron microscopy by Zhang et al., (2016).

The mechanisms and structural lattice changes induced by incorporating early oxygen atoms are of interest to fully understand how oxidation and saturation of oxygen covers a surface. To study this, simulations of surface core level shifts must be performed to understand on what surfaces of a crystal lattice changes become generated by the incorporation of oxygen atoms.

References

Atrens, A., Shi, Z., Mehreen, S.U., Johnston, S., Song, G-L., Chen, X., Pan, F. (2020). Review of Mg alloy corrosion rates, Journal of Magnesium and Alloys, Vol.8, Issue 4, 2020, pp. 989-998. DOI: https://doi.org/10.1016/j.jma.2020.08.002.

Bakhsheshi-Rad, H.. Hamzah, E.. Fereidouni-Lotfabadi, A.. Daroonparvar, M.. Yajid, M.. Mezbahul-Islam, M.. Kasiri-Asgarani, M.. Medraj, M. Microstructure and bio-corrosion behavior of Mg–Zn and Mg–Zn–Ca alloys for biomedical applications. Mater. Corros. 2014, 65, 1178–1187 https://doi.org/10.1002/maco.201307588

Bakhsheshi-Rad, H.. Hamzah, E.. Medraj, M.. Idris, M.. Lotfabadi, A.. Daroonparvar, M.. Yajid, M. Effect of heat treatment on the microstructure and corrosion behaviour of Mg–Zn alloys. Mater. Corros. 2014, 65, 999–1006 https://doi.org/10.1002/maco.201307492

Bhan, S., & Lal, A. (1993). The Mg-Zn-Zr system (magnesium-zinc-zirconium). *Journal of Phase Equilibria, 14*, 634-637.

Biotronik AG, https://www.biotronik.com/en-de/products/coronary/magmaris [accessed 2023-04-13]

Bornapour. M., Mahjoubi. H., Vali. H., Shum-Tim. D., Cerruti. M., Pekguleryuz. M., (2016) Surface characterization, in vitro and in vivo biocompatibility of Mg-0.3Sr-0.3Ca for temporary cardiovascular implant, Materials Science and Engineering: C., Volume 67. 2016. pp 72-84. https://doi.org/10.1016/j.msec.2016.04.108

Cai, S.. Lei, T.. Li, N.. Feng, F. Effects of Zn on microstructure, mechanical properties and corrosion behavior of Mg–Zn alloys. Mater. Sci. Eng. C 2012, 32, 2570–2577 https://doi.org/10.1016/j.msec.2012.07.042

Cao, F.. Shi, Z.. Song, G.-L.. Liu, M.. Atrens, A. Corrosion behaviour in salt spray and in 3.5% NaCl solution saturated with $Mg(OH)_2$ of as-cast and solution heat-treated binary Mg–X alloys: X = Mn, Sn, Ca, Zn, Al, Zr, Si, Sr. Corros. Sci. 2013, 76, 60–97. https://doi.org/10.1016/j.corsci.2013.06.030

Chen, X.-B.. Kirkland, N.. Krebs, H.. Thiriat, M.. Virtanen, S.. Nisbet, D.. Birbilis, N. In vitro corrosion survey of Mg–x Ca and Mg–3Zn–y Ca alloys with and without calcium phosphate conversion coatings. Corros. Eng. Sci. Techn. 2012, 47, 365–373 https://doi.org/10.1179/1743278212Y.0000000019

Chen, Y., Xu, Z., Smith, C., & Sankar, J. (2019). Recent advances on the development of magnesium alloys for biodegradable implants. Acta Biomaterialia, 88, 1-26.

El-Rahman, Sahar S.Abd, (2003) Neuropathology of aluminum toxicity in rats (glutamate and GABA impairment), Pharmacological Research,Volume 47, Issue 3,2003,189-194, https://doi.org/10.1016/S1043-6618(02)00336-5

Esmaily, M., Svensson, J., Fajardo, S., Birbilis, N., Frankel, G., Virtanen, S., Arrabal, R., Thomas, S., Johansson, L. (2017). Fundamentals and advances in magnesium alloy corrosion. Progress in Materials Science, vol. 89, 2017, pp.92-193.

Fragkakis, A., (2023) Studying the effects of chemical composition & microstructure on mechanical properties and corrosion of bio-degradable Mg-alloys. Internship Report, Mechanics, Materials and Component Design, LTH, Lund University.

Frost, HM. (1994). Wolff's Law and bone's structural adaptations to mechanical usage: an overview for clinicians. The Angle Orthodontist. 64 (3): 175–188. PMID 8060014.

Gao, J.. Guan, S.. Ren, Z.. Sun, Y.. Zhu, S.. Wang, B. Homogeneous corrosion of high pressure torsion treated Mg–Zn–Ca alloy in simulated body fluid. Mater. Lett. 2011, 65, 691–693 https://doi.org/10.1016/j.matlet.2010.11.015

Goldstein, J. I., Newbury, D.E., Echlin, P., Joy, D.C., Romig Jr, A.D., Lyman C.E., … & Lifshin, E. (2003) Scanning electron microscopy and x-ray microanalysis (3rd ed.). Springer.

Guan, R-g., Cipriano, A. F., Zhao, Z-y., Lock, J., Tie, D., Zhao, T., Cui, T., Liu, H. (2013) Development and evaluation of a magnesium–zinc–strontium alloy for biomedical applications —Alloy processing, microstructure, mechanical properties, and biodegradation, Materials Science and Engineering: C, vol. 33, no. 7, pp. 3661–3669.

Ha, H.-Y.. Kang, J.-Y.. Yang, J.. Yim, C.D.. You, B.S. Limitations in the use of the potentiodynamic polarisation curves to investigate the effect of Zn on the corrosion behaviour of as-extruded Mg–Zn binary alloy. Corros. Sci. 2013, 75, 426–433 https://doi.org/10.1016/j.corsci.2013.06.027

Ibrahim, H.. Klarner, A.D.. Poorganji, B.. Dean, D.. Luo, A.A.. Elahinia, M. Microstructural, mechanical and corrosion characteristics of heat-treated Mg-1.2 Zn-0.5 Ca (wt%) alloy for use as resorbable bone fixation material. J. Mech. Behav. Biomed. 2017, 69, 203–212 https://doi.org/10.1016/j.jmbbm.2017.01.005

Jiang, P., Blawert, C., & Zheludkevich, M. L. (2020). The Corrosion Performance and Mechanical Properties of Mg-Zn Based Alloys—A Review. Corrosion and Materials Degradation, 1(1), 92–158. MDPI AG. http://dx.doi.org/10.3390/cmd1010007

Koç, E.. Kannan, M.B.. Ünal, M.. Candan, E. Influence of zinc on the microstructure, mechanical properties and in vitro corrosion behavior of magnesium–zinc binary alloys. J. Alloys Compd. 2015, 648, 291–296 https://doi.org/10.1016/j.jallcom.2015.06.227

Kubasek, J.. Vojtěch, D. Structural characteristics and corrosion behavior of biodegradable Mg–Zn, Mg–Zn–Gd alloys. J. Mater. Sci. Mater. Med. 2013, 24, 1615–1626 https://doi.org/10.1007/s10856-013-4916-3

Li, H.. Liu, D.. Zhao, Y.. Jin, F.. Chen, M. The influence of Zn content on the corrosion and wear performance of Mg-Zn-Ca alloy in simulated body fluid. J. Mater. Eng. Perform. 2016, 25, 3890–3895
https://doi.org/10.1007/s11665-016-2207-0

Liu, M., Qiu, D., Zhao, M.-C., Song, G., Atrens, A. (2008) The effect of crystallographic orientation on the active corrosion of pure magnesium. Scripta Materialia 58, 2008, pp. 421-424. https://doi.org/10.1016/j.scriptamat.2007.10.027

Liu, X.-B.. Shan, D.-Y.. Song, Y.-W.. Han, E.-H. Effects of heat treatment on corrosion behaviors of Mg-3Zn magnesium alloy. T. Nonferr. Metal Soc. 2010, 20, 1345–1350. https://doi.org/10.1016/S1003-6326(09)60302-2

Lu, Y.. Bradshaw, A.. Chiu, Y.. Jones, I. Effects of secondary phase and grain size on the corrosion of biodegradable Mg–Zn–Ca alloys. Mater. Sci. Eng. C 2015, 48, 480–486 https://doi.org/10.1016/j.msec.2014.12.049

Maier, P. et al. (2019). Corrosion Bending Fatigue of RESOLOY® and WE43 Magnesium Alloy Wires. In: Joshi, V., Jordon, J., Orlov, D., Neelameggham, N. (eds) Magnesium Technology 2019. The Minerals, Metals & Materials Series. Springer, Cham. https://doi.org/10.1007/978-3-030-05789-3_26

McCall, C.R., Hill, M.A., Lillard, R.S. (2005) Crystallographic pitting in magnesium single crystals. Corros. Eng. Sci. Technol.2005, 40, 337–343. https://doi.org/10.1179/174327805X66326

McDonald, S., Reischig, P., Holzner, C., Lauridsen, E.M., Withers, P.J., Merkle, A.P., Feser, M. (2015) Non-destructive mapping of grain orientations in 3D by laboratory X-ray microscopy. Sci Rep 5, 14665 (2015). https://doi.org/10.1038/srep14665

Mei, D., Lamaka, S.V., Lu, X., Zheludkevich, M.L. Selecting medium for corrosion testing of bioabsorbable magnesium and other metals – A critical review. (2020) Journal of Corrosion Science. Vol. 171 2020. https://doi.org/10.1016/j.corsci.2020.108722

Nayak, S.. Bhushan, B.. Jayaganthan, R.. Gopinath, P.. Agarwal, R.. Lahiri, D. Strengthening of Mg based alloy through grain refinement for orthopaedic application. J. Mech. Behav. Biomed. 2016, 59, 57–70 https://doi.org/10.1016/j.jmbbm.2015.12.010

Orlov, D. *et al.* (2020). Advanced Immersion Testing of Model Mg-Alloys for Biomedical Applications. In: Jordon, J., Miller, V., Joshi, V., Neelameggham, N. (eds) Magnesium Technology 2020. The Minerals, Metals & Materials Series. Springer, Cham. https://doi.org/10.1007/978-3-030-36647-6_37

Orlov, D., Ralston, K. D., Birbilis, N. & Estrin, Y. (2011) Enhanced corrosion resistance of Mg alloy ZK60 after processing by integrated extrusion and equal channel angular pressing. Acta Materialia 59, 6176–6186 (2011). https://doi.org:10.1016/j.actamat.2011.06.033

Orlov, D., Viklund, M., Wadsö, L. (2022). Novel Laboratory-Scale In Situ Methods for Studying Mg Alloy Degradation. In: Maier, P., Barela, S., Miller, V.M., Neelameggham, N.R. (eds) Magnesium Technology 2022. The Minerals, Metals & Materials Series. Springer, Cham. https://doi.org/10.1007/978-3-030-92533-8_43

Polmear, I., StJohn, D., Nie, J.F., Qian, M. (2017). Light alloys: Metallurgy of the light metals (5th ed.). Elsevier. pp 287 – 367, ISBN 978-08-099431-4.

Reimer, L., & Kohl, H. (2008). Transmission electron microscopy: physics of image formation. Springer Science & Business Media.

Schröder, E., Fasel, R., Kiejna, A. (2004) Mg(0001) surface oxidation: A two-dimensional oxide phase. Physical Review B. vol. 69, 193405. https://doi.org/10.1103/PhysRevB.69.193405 .

Shi, B., Yang, C., Peng, Y., Zhang, F., Pan, F. (2022) Anisotropy of wrought magnesium alloys: A focused overview, Journal of Magnesium and Alloys, Volume 10, Issue 6, 2022, Pages 1476-1510, https://doi.org/10.1016/j.jma.2022.03.006.

Shi, Z., Hofstetter, J., Cao, F., Uggowitzer, P.J., Dargusch, M. S., Atrens, A. (2015) Corrosion and stress corrosion cracking of ultra-high-purity Mg5Zn, Corrosion Science, vol. 93, 2015, pp. 330–335. https://doi.org/10.1016/j.corsci.2015.01.032.

Shin, K.S.; Bian, M.Z.; Nam, N.D. (2012) Effects of crystallographic orientation on corrosion behavior of magnesium single crys. JOM. 2012, 64, 664–670. https://doi.org/10.1007/s11837-012-0334-0

Song,G.-L. (2011) 1 - Corrosion electrochemistry of magnesium (Mg) and its alloys, Woodhead Publishing Series, Metals and Surface Engineering, Corrosion of Magnesium Alloys, Woodhead Publishing, 2011, pp. 3-65, ISBN 9781845697082, https://doi.org/10.1533/9780857091413.1.3

Song, G-L., Mishra, R., Xu, Z-Q. (2010) Crystallographic orientation and electrochemical activity of AZ31 Mg alloy. Electrochemistry Communications, Vol 12. Issue 8. 2010. Pp. 1009-1012. https://doi.org/10.1016/j.elecom.2010.05.011.

Song, Y.. Han, E.-H.. Shan, D.. Yim, C.D.. You, B.S. The effect of Zn concentration on the corrosion behavior of Mg–xZn alloys. Corros. Sci. 2012, 65, 322–330 https://doi.org/10.1016/j.corsci.2012.08.037

Song, Y.. Han, E.-H.. Shan, D.. Yim, C.D.. You, B.S. The role of second phases in the corrosion behavior of Mg–5Zn alloy. Corros. Sci. 2012, 60, 238–245 https://doi.org/10.1016/j.corsci.2012.03.030

Staiger, M., Pietak, A., Huadmai, J. and Dias, G. (2006). Magnesium and its alloys as orthopedic biomaterials: A review. Biomaterials, 27(9), pp.1728-1734.

Sun, J., Bachmann, F., Oddershede, J., Lauridsen, E. (2022). Recent advances of lab-based diffraction contrast tomography – reconstruction sped benchmark testing and validations. *IOP Conf. Ser.: Mater. Sci. Eng.* **1249** 012045. https://doi.org/10.1088/1757-899X/1249/1/012045 .

Syntellix A.G., https://www.syntellixA.G.de/en/products/product-overview/all.html [accessed 2023-04-13]

Peng, Q.. Li, X.. Ma, N.. Liu, R.. Zhang, H. Effects of backward extrusion on mechanical and degradation properties of Mg–Zn biomaterial. J. Mech. Behav. Biomed. 2012, 10, 128–137. https://doi.org/10.1016/j.jmbbm.2012.02.024

U&I, https://inno-sys.net/sub02/list.php?ca_id=10 [accessed 2023-04-13]

Viklund, M. (2020) Degradation of model biomedical Mg alloys in aqueous media, Division of Materials Engineering, Department of Mechanical Engineering, Lund University 2020.

Wadsö, L. (2005). Applications of an eight-channel isothermal conduction calorimeter for cement hydration studies. Cement International, vol. Jg. 3, no. Nr. 5, pp. 94-101.

Williams, D.B., & Carter, C.B. (2009) Transmission electron microscopy: a textbook for materials science. Springer Science & Business Media.

Witte, F. (2015) Reprint of: The history of biodegradable magnesium implants: A review. Acta Biomaterialia 23, Supplement, S28-S40 (2015). https://doi.org:10.1016/j.actbio.2015.07.017

Witte, F., Kaese, V., Haferkamp, H., Switzer, E., Meyer-Lindenberg, A., Wirth, C. and Windhagen, H. (2005). In vivo corrosion of four magnesium alloys and the associated bone response. Biomaterials, 26(17), pp.3557-3563.

Xnovo technology ApS https://xnovotech.com/ [latest accessed 2023-04-21].

Yan, Y.. Cao, H.. Kang, Y.. Yu, K.. Xiao, T.. Luo, J.. Deng, Y.. Fang, H.. Xiong, H.. Dai, Y. Effects of Zn concentration and heat treatment on the microstructure, mechanical properties and corrosion behavior of as-extruded Mg-Zn alloys produced by powder metallurgy. J. Alloys Compd. 2017, 693, 1277–1289 https://doi.org/10.1016/j.jallcom.2016.10.017

Zander, D.. Zumdick, N.A. Influence of Ca and Zn on the microstructure and corrosion of biodegradable Mg–Ca–Zn alloys. Corros. Sci. 2015, 93, 222–233. https://doi.org/10.1016/j.corsci.2015.01.027

Zhang, B.. Wang, Y.. Geng, L. Research on Mg-Zn-Ca alloy as degradable biomaterial. In Biomaterials-Physics and Chemistry. Pignatello, R., Ed.. InTech: London, UK, 2011. pp. 183–204 https://doi.org/10.1016/j.msec.2011.07.015

Zhang, B.. Hou, Y.. Wang, X.. Wang, Y.. Geng, L. Mechanical properties, degradation performance and cytotoxicity of Mg–Zn–Ca biomedical alloys with different compositions. Mater. Sci. Eng. C 2011, 31, 1667–1673

Zhang, B.. Wang, Y.. Geng, L.. Lu, C. Effects of calcium on texture and mechanical properties of hot-extruded Mg–Zn–Ca alloys. Mater. Sci. Eng. A 2012, 539, 56–60. https://doi.org/10.1016/j.msea.2012.01.030

Zhang, E., Xu, L., Yu, G., Pan, F., Yang, K., & Li, Y. (2014). Research progress on the use of magnesium alloys in biomedical applications. Biomedical Materials, 9(3), 034005.

Zhang, S., Li, M., Li, J., Li, P., Sun, Y., Zhang, X., ... & Jiang, Y. (2017). Biodegradable magnesium alloys developed as bone repair materials: A review. Scanning, 2017, 8956208.

Zhang, S.. Zhang, X.. Zhao, C.. Li, J.. Song, Y.. Xie, C.. Tao, H.. Zhang, Y.. He, Y.. Jiang, Y. Research on an Mg–Zn alloy as a degradable biomaterial. Acta Biomater. 2010, 6, 626–640. https://doi.org/10.1016/j.actbio.2009.06.028

Zhang, S.. Zheng, Y.. Zhang, L.. Bi, Y.. Li, J.. Liu, J.. Yu, Y.. Guo, H.. Li, Y. In vitro and in vivo corrosion and histocompatibility of pure Mg and a Mg-6Zn alloy as urinary implants in rat model. Mater. Sci. Eng. C 2016, 68, 414–422. https://doi.org/10.1016/j.msec.2016.06.017

Zhang, Z., Fu, X., Mao, M., Yu, Q., Mao, S.X., Li, J., Zhang, Z. (2016) *In situ* observation of sublimation-enhanced magnesium oxidation at elevated temperature. Nano Research 2016, 9(9): pp. 2796-2802. https://doi.org/10.1007/s12274-016-1168-9

Zheng, Y.. Li, Y.. Chen, J.. Zou, Z. Effects of tensile and compressive deformation on corrosion behaviour of a Mg–Zn alloy. Corros. Sci. 2015, 90, 445–450. https://doi.org/10.1016/j.corsci.2014.10.043

Appendix 1 – Isothermal Calorimetry data

Sample sizes for calorimetric measurements are presented in table A1

Each dimension was measured five times, maximum and minimum values were considered outliers and excluded, marked by a line through the value (e.g.: ~~3.54~~). The Average for each dimension were calculated and the surface area of the sample were calculated from these averages. All dimensions are in mm, Area given in mm^2.

Table A1.1: Measurements, averages and calculated surface area for samples used in isothermal calorimetry. All singleton dimensions are in mm. area in mm^2. Sample #3 in Z5 SSSS was excluded due to gas leak, indicated by the strike through of all values.

Z5 AS	Width		Length		Thickness		Surface area
Sample #	Meas.	Avg.	Meas.	Avg.	Meas.	Avg.	
1	3.62 3.60 ~~3.54~~ 3.60 ~~3.62~~	3.61	~~9.54~~ 9.54 ~~9.62~~ 9.59 9.58	9.57	1.94 1.94 1.94 ~~1.95~~ ~~1.94~~	1.94	120.23
2	~~3.55~~ 3.52 3.54 ~~3.49~~ 3.53	3.53	~~9.24~~ 9.35 9.37 9.39 ~~9.39~~	9.37	~~2.11~~ 2.16 ~~2.18~~ 2.16 2.16	2.16	121.88
3	3.79 3.78 ~~3.76~~ ~~3.83~~ 3.82	3.80	~~9.53~~ ~~9.69~~ 9.58 9.61 9.63	9.61	~~1.81~~ ~~1.79~~ 1.79 1.81 1.81	1.80	121.31
4	~~3.57~~ 3.55 ~~3.51~~ 3.55 3.52	3.54	~~9.14~~ 9.16 ~~9.21~~ 9.19 9.20	9.18	~~2.00~~ 2.02 2.04 2.03 ~~2.05~~	2.03	116.64

Z5 SSSS	Width		Length		Thickness		Surface area
Sample #	Meas.	Avg.	Meas.	Avg.	Meas.	Avg.	
1	5.98 ~~5.97~~ 6.00 6.00 ~~6.01~~	5.99	~~9.66~~ 9.68 9.69 ~~9.70~~ 9.67	9.68	0.60 0.60 ~~0.61~~ 0.60 ~~0.60~~	0.60	134.77
2	~~9.68~~ 9.63 9.65 9.68 ~~9.62~~	9.65	~~13.16~~ 13.23 13.23 13.19 ~~13.31~~	13.22	0.88 ~~0.87~~ 0.89 0.90 ~~0.90~~	0.89	295.85
~~3~~	~~10.93~~ ~~10.92~~ ~~10.95~~ ~~10.96~~ ~~10.98~~	~~10.95~~	~~10.42~~ ~~10.44~~ ~~10.41~~ ~~10.44~~ ~~10.41~~	~~10.42~~	~~0.20~~ ~~0.22~~ ~~0.19~~ ~~0.18~~ ~~0.19~~	~~0.19~~	~~236.32~~
4	~~8.15~~ 8.34 ~~8.38~~ 8.25 8.30	8.30	~~9.56~~ 9.59 9.62 9.61 ~~9.63~~	9.61	0.83 ~~0.81~~ ~~0.88~~ 0.87 0.87	0.86	190.33

ZX50	Width		Length		Thickness		Surface area
Sample #	Meas.	Avg.	Meas.	Avg.	Meas.	Avg.	
1	5.44 5.38 5.35 ~~5.45~~ ~~5.33~~	5.39	9.50 9.42 ~~9.64~~ 9.58 ~~9.41~~	9.50	~~1.37~~ ~~1.38~~ 1.38 1.37 1.37	1.37	143.20
2	~~5.37~~ 5.42 ~~5.47~~ 5.42 5.46	5.43	9.63 ~~9.55~~ 9.61 9.58 ~~9.67~~	9.61	0.94 ~~0.91~~ 0.93 0.94 ~~0.94~~	0.94	132.64

Raw data of calorimetric runs are presented in figure A.1 below. A drop off in pressure can be noted for Z5 SSSS channel 6 (Figure A1.1 B), this channel was excluded in the analysis in this work. In data for ZX50 (Figure A1.1 C) only channels 1 and 3 were used as channels 6 and 8 were used for another experiment on another material. Since the calorimeter handles each channel individually, parallel experiments at the same temperature do not interfere with each other.

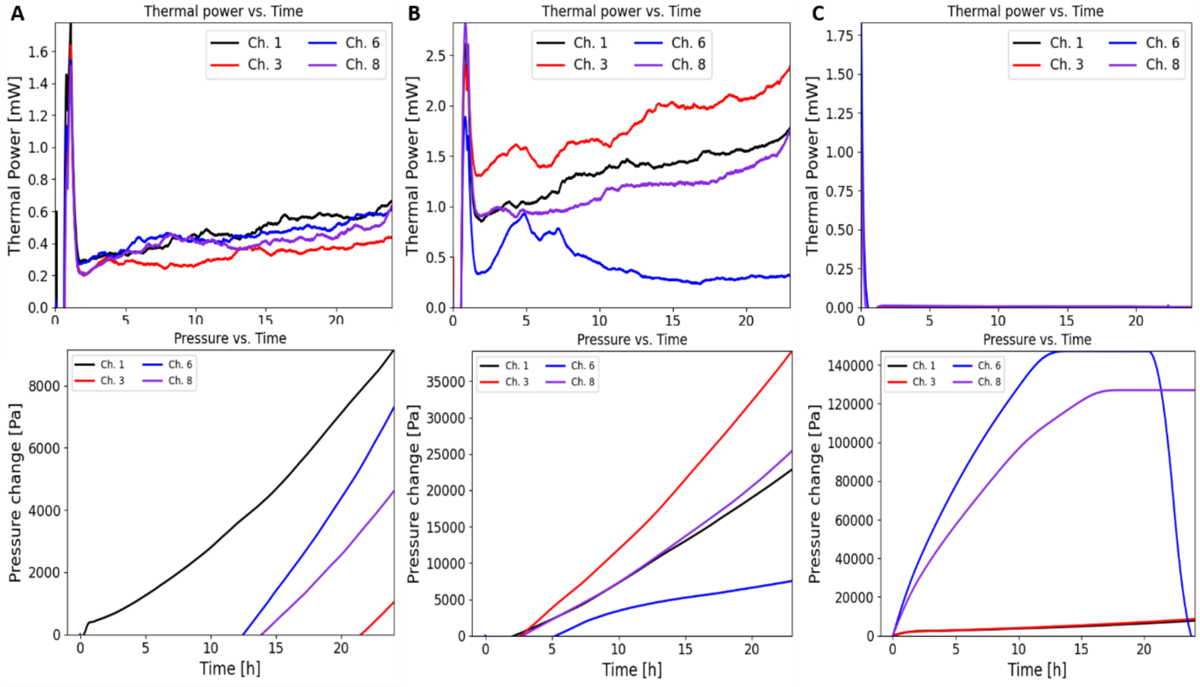

Figure A1.1: Raw data of calorimetric runs. Thermal power in top row, pressure bottom row. A: Z5 AS, B: Z5 SSSS, C: ZX50. In C, ZX50, channel 6 and are from a parallel experiment of another material and should be disregarded.

Note that in figure A1.1 the pressure for both Z5 materials starts negative. This is due to the calibration of pressure sensor being relative to pressure changes and not absolute pressure. The diagrams are forced to plot from 0 Pa hence some data that is later used in calculations is not visible in the raw data plots.

Appendix 2- Matlab code for extracting slices of reconstructed volume.

The matlab code to visualize slices of the reconstructed volume is presented here. The code builds of and requires the MTEX toolbox to run.

```
%% Plotting slices from DCT (.h5) files.
% import filepath:
importfile='C:\Users\user\Documents\Johan\DCT\Z5\AS\DymtroZ5-
AS_160223_export.h5';

% Define Crystal symmetry ( see [help crystalSymmetry] for namelist etc)
cs=crystalSymmetry('D6h');

% Choose plane to analyze X ([YZ]) Y ([XZ]) or Z ([XY]) plane:
P='Y';
assert(ismember(P,['X','Y','Z']),'P must be either ''X'',''Y'', or ''Z''');

% importing data, do not alter.
EulAng = h5read(importfile,'/LabDCT/Data/EulerZXZ');
GRAINS = h5read(importfile,'/LabDCT/Data/GrainId');

% choose what slice to analyze, either by setting a value to thisSlice or
% by choosing absorption slice out of total ammount abs slices, in chosen
% plane, remember to move index 'thisSlice' to correct position.
AS=652;  % absorption slice with corr attack.
AST=1012; % Total number of absorption silces.
% get size of dataset, limi =x, limj=y, limk=z.
[limuvw,limx,limy,limz]=size(EulAng);
% Below::use limk for XY plane, limj for XZ, limi for YZ plane.
thisSlice=ceil(limy*AS/AST);    % Slice in plane

% thisSlice=50; % used for testing since slice 50 exists in all datasets &
planes

% Visualize symmetry if needed by removing commented field below
% sR=cs.fundamentalSector;
% figure(1)
% plotb2west
% hold on
% plot(cs)
% hold off
% figure(2)
% plot(sR)


%% Visualize the slice in grayscale
if P == 'X'
 GRAINSsq=squeeze(GRAINS(thisSlice,:,:));
elseif P=='Y'
    GRAINSsq=squeeze(GRAINS(:,thisSlice,:));
elseif P=='Z'
    GRAINSsq=GRAINS(:,:,thisSlice);
end
figure(3)
 imshow(GRAINSsq,[0 15])

%% Define Orientation & Rotation
```

```
% If statement picks slice in plane P (X Y or Z), squeeze removes dimension
P to get matrix: (rot,axis1,axis2).
% then picks out rotations phi1 PHI phi2 from squeezed matrix.
if P=='X'
    EulAngSlice=EulAng(:,thisSlice,:,:);
    EulAngSq=squeeze(EulAngSlice(:,1,:,:));

    phi1= EulAngSq(1,:,:);
    PHI = EulAngSq(2,:,:);
    phi2= EulAngSq(3,:,:);

elseif P=='Y'
    EulAngSlice=EulAng(:,:,thisSlice,:);
    EulAngSq=squeeze(EulAngSlice(:,:,1,:));

    phi1= EulAngSq(1,:,:);
    PHI = EulAngSq(2,:,:);
    phi2= EulAngSq(3,:,:);

elseif P=='Z'
    EulAngSlice=EulAng(:,:,:,thisSlice);
    EulAngSq=squeeze(EulAngSlice(:,:,:,1));

    phi1= EulAngSq(1,:,:);
    PHI = EulAngSq(2,:,:);
    phi2= EulAngSq(3,:,:);
end

rot=rotation.byEuler(phi1,PHI,phi2,'Bunge'); % define angles and rotation
convention

%% set image mesh
% change limits to match the plane you are working in!
% XY plane uses meshgrid(1:limy, 1:limx)
% XZ plane uses meshgrid(1:limz, 1:limx)
% YZ plane uses meshgrid(1:limz, 1:limy)
if P=='X'
    [X,Y]=meshgrid(1:limz,1:limy);
elseif P=='Y'

    [X,Y]=meshgrid(1:limz,1:limx);
elseif P=='Z'

    [X,Y]=meshgrid(1:limy,1:limx);
end

X=X(:);
Y=Y(:);
prop.x=X;
prop.y=Y;

% indexing what symmetries are present index 1: not indexed, index 2:
% indexed as crystal symmetry
CSlist={'notIndexed',cs};

% Determine that voxels with grainID = 0 are not indexed.
% complimentary to CSlist.
```

```
   if P=='X'
       GRAINSslice=GRAINS(thisSlice,:,:);
       GRAINSslice=squeeze(GRAINSslice(1,:,:));
   elseif P=='Y'
       GRAINSslice=GRAINS(:,thisSlice,:);
       GRAINSslice=squeeze(GRAINSslice(:,1,:));
   elseif P=='Z'
       GRAINSslice=GRAINS(:,:,thisSlice);
       GRAINSslice=squeeze(GRAINSslice(:,:,1));
   end

phaseId=logical(GRAINSslice(:));

ebsd = EBSD(rot,phaseId,CSlist,prop); % make a EBSD slice of the selected
slice
%ebsd.grainId=double(GRAINS(:,:,thisSlice));

%% Calculate grain boundaries
cS = crystalShape.hex(ebsd.CS);
[grains,ebsd.grainId] = calcGrains(ebsd('indexed'));
% remove all very small grains
ebsd(grains(grains.grainSize < 5)) = [];
% 3. redo grain reconstruction
[grains,ebsd.grainId] = calcGrains(ebsd('indexed'));
big_grains = grains(grains.grainSize > 50);

%% Plot slice

ipfkey=ipfHSVKey(cs); % import colormap
rgb=ipfkey.orientation2color(ebsd.orientations);  % apply colormap to
rotations
figure(4)
plot(ebsd,ebsd.orientations,'micronbar','off')
%% test segment, plots overlaid unit cells.
% plots reconstruction with overlay unit cells.
% re-does reconstruction, bad?
grains = smooth(grains,4);

figure(5)
plot(ebsd,ebsd.orientations,'micronbar','off')
hold on
plot(grains.boundary,'lineWidth',2,'micronbar','off')
plot(big_grains,0.5*cS,'linewidth',2,'FaceColor','none')
hold off

%% Plot IPF
figure(6)
plotIPDF(ebsd.orientations,rgb,[xvector yvector
zvector],'MarkerSize',10,'markerEdgeColor','k','antipodal','all')

figure(7)
plot(ipfkey,'fundamentalRegion','upper')
```